Tang T. & Huang L. (2022). An efficient semi-analytical procedure to calculate acoustic radiation force and torque for axisymmetric irregular bodies. Journal of Sound a*nd Vibration*.
DOI: 10.1016/j.jsv.2022.117012

An efficient semi-analytical procedure to calculate acoustic radiation force and torque for axisymmetric irregular bodies

Tianquan Tang[a,b,*], Lixi Huang[a,b]

[a]*Department of Mechanical Engineering, The University of Hong Kong, Pokfulam, Hong Kong SAR, China*
[b]*Lab for Aerodynamics and Acoustics, HKU Zhejiang Institute of Research and Innovation, 1623 Dayuan Road, Lin An District, Hangzhou, China*

* Corresponding email: tianquan@connect.hku.hk.

With the attributes of being biocompatible, label-free, and contact-free, sound has been widely used to manipulate micro-objects, such as cells, soft matters, and living things, by the acoustic radiation force and torque arising from wave scattering. The analytical theory exists for the acoustic radiation force and torque on separable geometries, including sphere and ellipsoid. However, it is still a challenge to handle irregular surfaces subject to non-orthogonal and inseparable boundary conditions. Here, we present a calculation method for an axisymmetric geometry with irregular cross-section excited by a time-harmonic plane wave with arbitrary incidence in the inviscid fluid. The method is based on conformal mapping from the irregular surface to a sphere in the new coordinate system. In this way, the separation of variables can be used to solve the corresponding Helmholtz wave equation subjecting to the spherical boundary conditions in the new coordinate system. The radiation force and the torque are asymptotically obtained using the far-field, closed-form solutions. The method is validated by comparisons with full 3D numerical solutions over a wide range of frequencies and incident angles. With a typical discrepancy of less than 5%, the proposed method is much more efficient than the full numerical simulations (*via* finite element method). Furthermore, it is found that the radiation force acting on different geometries follows the same tendency. The difference is that the presence of the

radiation torque ensures that the symmetry axis of the irregular bodies is coincident with or orthogonal to the wave propagating direction.

Keywords: Acoustic radiation force, Acoustic radiation torque, Conformal transformation, Axisymmetric irregular geometries

1. Introduction

The manipulation of microparticles is essential for particle separation [1][2], agglomeration [3][4], transport [5][6][7][8], pattern formation [9][10][11], and imaging [12][13][14][15]. These applications potentially promote the biochemistry and medical industries in specific subjects, including migration of microorganisms [16], assembly of colloidal structure [17], and development of novel bioprinting method [18]. Various techniques, such as magnetic [19], optical [20][21], and acoustic [7], can spatially contactless manipulation of particles. However, the magnetic and electronic techniques require the particles or media to be magnetically susceptible or electrically polarizable. Optical alternatives are limited by sample damage due to extensive heating by lasers [22]. By contrast, acoustic methods are free from such constraints, and have superior efficiency and low-power operation [23], thereby preventing excessive heat from deactivating organisms. Acoustic waves exert acoustic radiation force and torque on objects because of the momentum transfer that arises from acoustic scattering effects of the wave-particle interaction [24][25][26][27]; these second-order force and torque, caused by inherent nonlinearities in the governing physics [28], manipulate the behavior of the objects. The careful control of these effects enables handling particles ranged from 1 μm [29] to 1 cm [30][31] in a contactless manner.

For Rayleigh particles, where the scattering effect is negligible, the acoustic radiation force on the particles due to the known incident fields can be easily evaluated according to Gorkov's theory [32]. In this way, the particles are typically trapped at the pressure nodes of incident driving fields [5][7][33]. By contrast, the effect of the acoustic radiation torque on these Rayleigh particles is insignificant [34], thereby attracting less attention.

Beyond the Rayleigh regime, the complex scattering phenomena become considerable. The partial wave expansion is a powerful and effective tool in describing the scattering fields [35]. For a single sphere system, starting from the partial wave expansion of the incident and scattered waves in the spherical coordinate system, the analytical expressions of the acoustic radiation force and torque are derived concerning the expansion coefficients. The boundary conditions of the spherical particles and the

orthogonality of the spherical wavefunctions (the basis functions) are employed to decouple each mode and obtain a system of linear equations for the unknown scattering expansion coefficients [36][37]. Additionally, for the multi-sphere system, the acoustic radiation interaction force and torque among particles excited by the plane waves [38] or the ultrasonic transducer arrays [39] have been developed with the help of the translation addition theorem [40].

An obvious limitation of the above studies is that they all assumed the manipulated object(s) to be spherical. In reality, most objects have a certain degree of asymmetry in their morphology, such as *erythrocyte* [41] and *C. elegans* [42]. When considering a prolate spheroidal object, the radial distance to the locus of any point on the object surface depends on the angular coordinates. Consequently, the spherical wavefunctions are not necessarily orthogonal, which renders closed-form exact solutions of the scattering expansion coefficients for the radiation force and torque as difficult to be attained on the spherical coordinate system. By introducing the surface shape function of spheroid to describe the boundary conditions, the resulting acoustic scattering field is obtainable [43][44]. Based on the derived scattering field, the radiation force on the prolate spheroids in Bessel beams can be estimated [45][46][47][48]. Similarly, the radiation force and torque exerted on specific corrugated circular and elliptical cylinders can be solved once the shape function is given [49]. Alternatively, this difficulty could also be bypassed if (i) the radiation force and torque are calculated through the far-field method where the radiation stress is integrated on a far-field spherical control surface [24][26], and (ii) the incident and scattered partial wave expansions (precisely, the spherical Bessel and Hankel functions [35]) in spheroidal coordinate system asymptotically match the expansions in the spherical coordinate system at a far-field, an analytical solution of the acoustic radiation force and torque on a prolate spheroidal particle in plane waves with are able to obtain [50][51][52].

In fact, exact solutions can be found for only a limited class of geometries (separable geometries) where separation of variables is applicable. More specifically, the problem must be able to formulate in a specific coordinate system where the locus of points corresponding to one of the coordinates (typically, the radial coordinate) being a constant coincides with the scatterer surface. For example, sphere and ellipsoid are

mapped to the spherical and the spheroidal coordinate systems, respectively. In this way, the corresponding Helmholtz wave equation in the mapping coordinate system becomes separable. For irregular bodies (or inseparable bodies), where exact separation of variables is not possible, approximate analytical solutions, such as the perturbation method [53] and approximate asymptotic formulations [54][55], have been developed to model the wave-particle interaction. However, the former is only valid if the shape is close to one of the separable geometries, and the latter is designed to work in scenarios that the wavelength of the incident field is much smaller than the dimension of the scatterers. More importantly, these approximate methods are not formulated in spherical wavefunction series, meaning that the orthogonality of wavefunctions cannot be employed to eliminate the integration of acoustic velocity potential fields in solving radiation force and torque analytically. An available alternative to model the radiation force and torque on the irregular bodies is the use of numerical techniques [41][56], while it is limited by high computational cost. Furthermore, it is impractical to dynamically analyze the motion of the objects if the object state varies continuously. A general analytical result to evaluate the acoustic radiation torque on an irregular body was presented by Fan [57]. However, this investigation mainly focused on established a general theoretical framework of the acoustic radiation torque in the long-wavelength limit and lacked discussion on the radiation force.

Our present work aims to present a general analytical solution for both the acoustic radiation force and torque imparted on different axisymmetric, irregular bodies caused by a traveling plane wave with arbitrary incidence. Conformal mapping is used to transform the physical surface of the geometries into a spherical surface under a new mapping quasi-spherical coordinate system [58][59][60]. In this way, the locus of all points corresponding to the new radial coordinate being constant coincides with the scatterer surface. Thus the boundary conditions are enforced easily. A set of spherical angular eigenfunctions (Eq. (16), [59][61]) are chosen to yield an approximate closed-form solution for the scattering expansion coefficients. Consider that the new mapping coordinate system is designed to asymptotically match the spherical coordinate system at the far-field, the acoustic radiation force and torque integrated on a far-field control surface under the spherical coordinate system (or the Cartesian coordinate system) can be asymptotically derived by employing the scattering expansion coefficients obtained

in the new coordinate system. This technique has been demonstrated to be a viable route for solving the acoustic radiation force and torque to manipulate the axisymmetric bodies with irregular cross-sections.

The rest of the paper is organized as follows. In Sec. 2, the theoretical basis for the formulations is presented. Based on conformal mapping transformation, we start with developing a new orthogonal coordinate system where the exterior of the irregular surface of the scatterers is defined by the new radial coordinate at $u = u_0 = 0$ in Sec. 2.1. In Sec. 2.2, the partial-wave series solution to the transformed Helmholtz equation is given. In Sec. 2.3, a set of spherical angular eigenfunctions [61] are introduced, multiplying and integrating over the boundary conditions to generate the system of equations, which is then solved for the scattering expansion coefficients (referred to Appendix C) and used to determine the scattering potential amplitude. In Sec. 2.4, the acoustic radiation force and torque are obtained by a surface integration of the particles using the potential amplitude developed in Sec. 2.3. In Sec. 3, the acoustic radiation force and torque excited by plane wave fields on several irregular bodies (including sphere, ellipsoid, cone, and diamond) over a wide range of frequencies and incident angles are presented, based on either theoretical method or full three-dimensional numerical simulations. Further discussion is given, followed by comprehensive validations. A summary is made in Sec. 4.

2. Theoretical model

Evaluation of the acoustic radiation force and torque, resulting from the momentum transfer that arises from sound scattering phenomena, on an inseparable, irregular body is complex because the scattering wave field is difficult to formulate along the line of separation of variables. For the separable geometries, the scattering wave field can be immediately obtained by applying the boundary conditions where the locus of the points can be simply expressed by one of the coordinates being a constant, coincided with the scatterer surface. Then, the acoustic radiation force and torque can be evaluated (such as the spherical particle [34] and the ellipsoidal particle [52]). However, the locus of the points on the axisymmetric, irregular scatterer surfaces is generally formulated by radial and polar angular coordinates. The challenge is to describe the irregular surface in a new mapping coordinate system, where the separation of variables can be applied in exactly the same way as the natural physical space with regular geometries.

2.1. Conformal mapping transformation

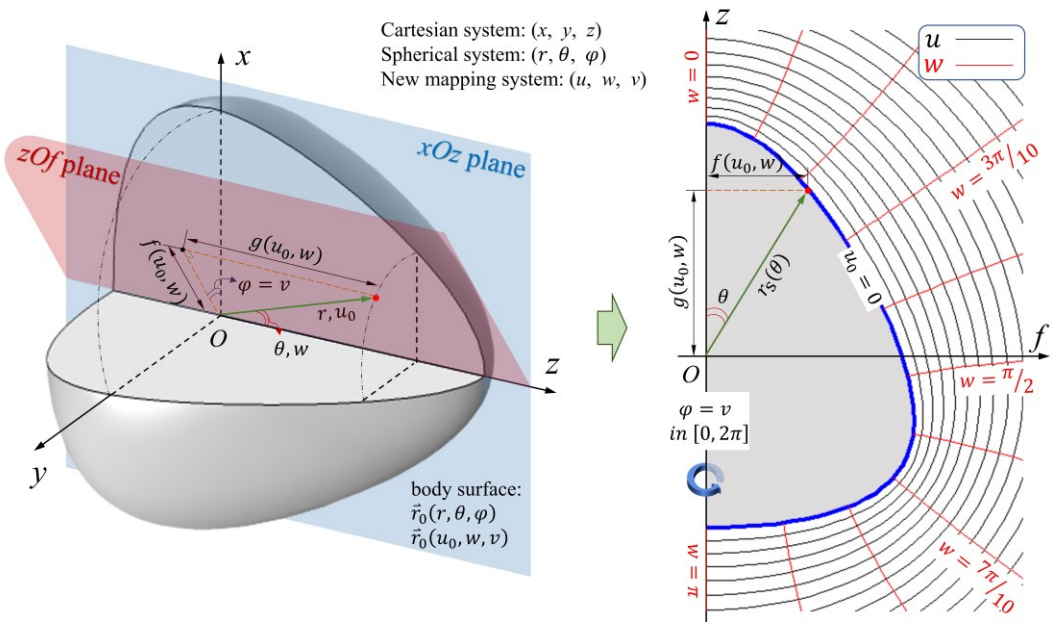

Figure 1: Mapping of the axisymmetric body with arbitrary profile contour. The body is symmetric about the z-axis. The surface position vector $\vec{r}_0(r,\theta,\varphi)$ is dependent on the radial coordinate, $r = r(\theta,\varphi)$, the polar angular coordinate, θ,

and the azimuthal angular coordinate, φ, in the spherical coordinate system. The body surface in the new mapped coordinate system of (u, w, v) can be described by the new radial coordinate $u = u_0 = 0$, independent with the new polar angular coordinate, w, and the new azimuthal angular coordinate, v. On the zOf slice plane (as marked by red in left-hand side sub-figure), the radial slice function, $r_s(\theta) = r_s(\theta, \varphi)$ can be described by the new coordinates of (u_0, w) as $r_s(\theta) = \sqrt{g^2(u_0, w) + f^2(u_0, w)}$ in the real-form, or $r_s(\theta) = g(u_0, w) + f(u_0, w) \cdot \mathrm{i}$ in the complex-form (the azimuthal angular coordinates, φ or v, are not involved for the axisymmetric reason). The mapping function $g(u_0, w)$ corresponds to the length along the z-axis, and mapping function $f(u_0, w)$ is the projection in the xy-plane.

Figure 1 shows the geometry and mapping information of an axisymmetric body on different coordinate systems. The center of mass of the irregular body is set to coincide with the origin of the Cartesian and the spherical coordinate systems. Conformal mapping transformation is used to map the irregular surface to a new quasi-spherical coordinate system of (u, w, v), namely the new mapping coordinate system, where the locus of all points on the body surface for the new radial coordinate, u, is equal to a constant, $u = u_0 = 0$. The new polar angular coordinate of the mapping coordinate system, w, corresponds to the spherical polar angular coordinate, θ. These two polar angular coordinates are not equal, while they can be mutually represented by the Fourier series on the body surface (Eq. (A.2)). For a body symmetric along the z-axis, the new azimuthal angular coordinate, v, remains identical with the spherical azimuthal angular coordinate φ, varied from 0 to 2π. Two mapping functions, $f(u, w)$ and $g(u, w)$, are introduced to trigonometry prescribe of the body surface, $u = u_0$, in the x, y and z directions of the Cartesian coordinate system

$$\begin{cases} x(u_0, w, v) = f(u_0, w) \cdot \cos(v) \\ y(u_0, w, v) = f(u_0, w) \cdot \sin(v) \\ z(u_0, w) = g(u_0, w) \end{cases}. \tag{1}$$

Note that the partial derivatives of the mapping functions should satisfy $f_u(u, w) = g_w(u, w)$ or $f_w(u, w) = -g_u(u, w)$ to achieve the orthogonality of the new coordinate system (Appendix B).

Consider that the axisymmetric property of the irregular body, the shape of the boundary of any cross-sectional slice for any specified azimuthal angle $\varphi \in [0, 2\pi]$ is

identical. Hence, the body surface can be regarded as a cross-sectional slice rotating along the azimuthal angular coordinate for a 2π period. We define the zOf plane to present the boundary of the cross-sectional slice as shown in Fig. 1. In this way, a general three-dimensional mapping is simplified to a two-dimensional mapping of (u, w) on the zOf plane with an independent new azimuthal angular coordinate v, which is identical to the azimuthal angular coordinate φ, i.e., $v = \varphi$. Specifically, we derive the following associated conformal mapping relationship on the body surface, $u = u_0$, as

$$\begin{cases} r_s(\theta) = r_s(u_0, w) = \sqrt{g^2(u_0, w) + f^2(u_0, w)} \\ \theta(u_0, w) = \cos^{-1}\left(g(u_0, w) \Big/ r_s(u_0, w)\right) \\ \varphi = v \end{cases}, \tag{2}$$

where $r_s(u_0, w)$ (or $r_s(\theta)$) is defined as the slice function, used to describe the boundary of the slice on the zOf plane.

As there should be only one value of the given slice function $r_s(\theta)$ for each θ, the mapping procedure for the axisymmetric body is commenced by expanding function $r_s(\theta)$ in a Fourier series relative to the polar angle, θ, as

$$r_s(\theta) = a + \sum_{n=1}^{\infty} [A_n \cos(n\theta) + B_n \sin(n\theta)], \tag{3}$$

where a is the average radius of the body, and A_n and B_n are the Fourier series coefficients. Note that the Fourier expansion is performed for the period of 2π, while the polar angular coordinate θ is defined from 0 to π. Consequently, although the series is intentionally computed based on the periodic extension from π to 2π, the polar angle is only meaningful in the range of $[0, \pi]$. Equation (3) can be rewritten in terms of exponentials as

$$r_s(\theta) = a + \sum_{n=1}^{\infty} \left[R_n^* e^{in\theta} + R_n e^{-in\theta}\right], \tag{4}$$

where $R_n = \frac{1}{2}(A_n + B_n)$ and the superscript symbol $*$ means taking conjugation of the corresponding variable. It is convenient to describe the boundary of the slice using the complex system

$$r_s(\theta) e^{\theta i} = a e^{\theta i} + \sum_{n=1}^{\infty} \left[R_n^* e^{i(1+n)\theta} + R_n e^{i(1-n)\theta}\right]. \tag{5}$$

The real part of $r_s(\theta)e^{i\theta}$ corresponds to the projection value of $r_s(\theta)$ in the z-axis and imaginary part of $r_s(\theta)e^{i\theta}$ is the projection value in f-axis for the real zOf slice plane.

Assume that the complex mapping function $M(u,w) = g(u,w) + f(u,w)\cdot i$ follows the conformal mapping form [58]

$$M(u,w) = c_{-1}e^{u+wi} + \sum_{n=0}^{\infty} c_n e^{-n(u+wi)}, \tag{6}$$

$$\begin{cases} g(u,w) = c_{-1}e^{u}\cos(w) + \sum_{n=0}^{\infty} c_n e^{-nu}\cos(nw) \\ f(u,w) = c_{-1}e^{u}\sin(w) - \sum_{n=0}^{\infty} c_n e^{-nu}\sin(nw) \end{cases},$$

where the mapping coefficients $c_n, n = -1,0,1,\cdots,\infty$ are used to map the boundary of the slice from the $(r_s(\theta),\theta)$ system to the $\big(g(u,w),f(u,w)\big)$ system. For a specific irregular body, a set of mapping coefficients can be determined by equating the slice function given in Eq. (5) to the mapping function $M(u,w)$ on the boundary of the slice with $u = u_0 = 0$, detailed in Appendix A. It can be found that the new coordinate system becomes a spherical coordinate system when the new radial coordinate tends to be infinite, $u \to \infty$. Consequently, the acoustic radiation force and torque evaluated using the far-field data are directly available to the existing results given in the new coordinate system without performing an inverse mapping.

Table 1: Mapping coefficients for various axisymmetric bodies in calculations. The average radius of these bodies is set to $a = 50$ μm.

Mapping coefficients	*Sphere*	*Ellipsoid*	*Cone*	*Diamond*
c_{-1}	a	a	a	a
c_0	0	0	0	0
c_1	0	$a/5$	0	0
c_2	0	0	$a/8$	0
c_3	0	0	0	$a/10$
$c_n, n>3$	0	0	0	0

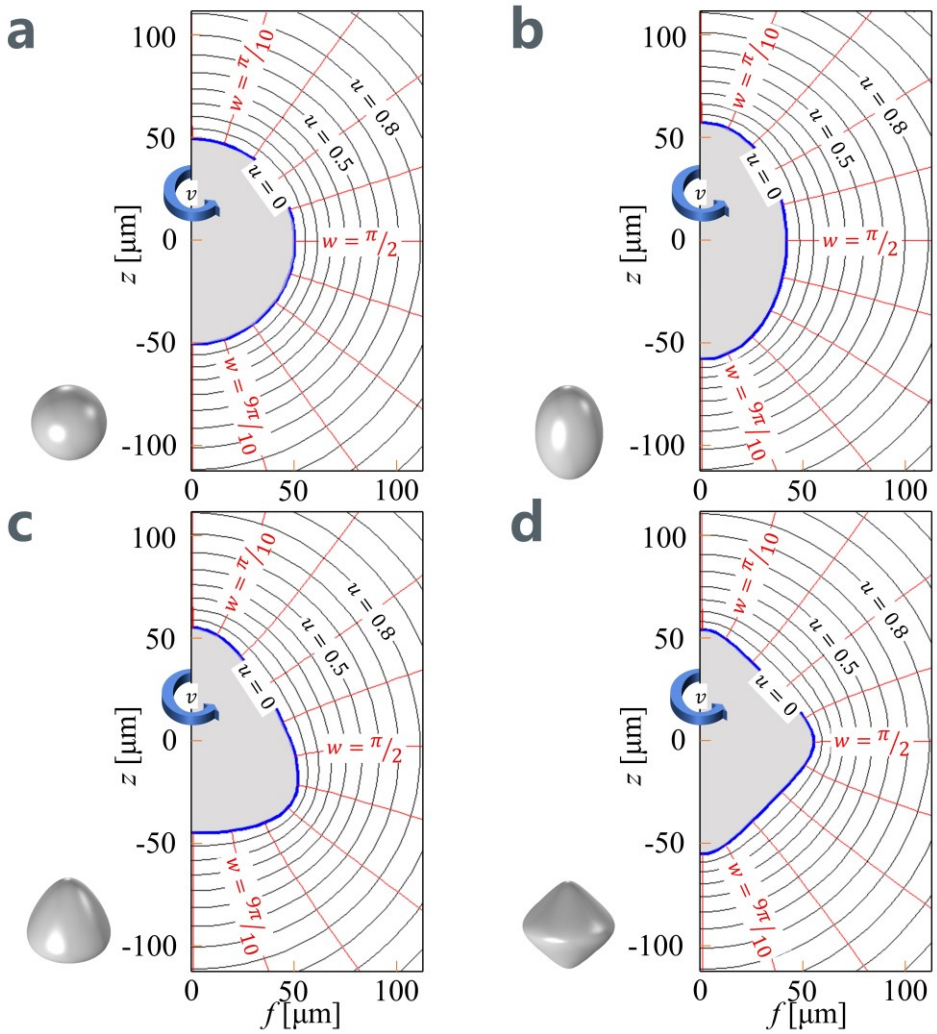

Figure 2: Visualization of the new orthogonal, axisymmetric coordinate systems for various irregular axisymmetric bodies. For the axisymmetric geometries, the three-dimensional conformal mapping procedure is reduced to a two-dimensional process between the zOf slice plane (defined and illustrated in Fig. 1) and the uw plane using Eqs. (1) and (6). Note that the three-dimensional conformal mapping between the spherical coordinate system, the $r\theta\varphi$ system, and the new coordinate system, the uwv system, can be immediately connected with the help of mapping functions, $g(u,w)$ and $f(u,w)$ (referred to Eq. (2)). The contours of the new radial coordinate u are plotted by solid black curves, while the contours of the new polar coordinate w are highlighted by solid red curves. Curves $u = 0, 0.5, 0.8$, and $w = \pi/10,\ \pi/2,\ 9\pi/10$ are emphasized, with the inner curve being $u = 0$ along the surface of the irregular bodies. The corresponding mapping coefficients used to define the new coordinate systems applicable to **a)** sphere, **b)** ellipsoid, **c)** cone, and **d)** diamond are specified in Tab. 1.

The mapping coefficients, c_n, for various irregular bodies are given in Tab. 1, and the corresponding mapping coordinate systems are shown in Fig. 2. It can be seen from Fig. 2 that the new coordinate system tends to be the spherical coordinate system with the increase of the new radial coordinate u.

2.2. Solution of the Helmholtz wave equation

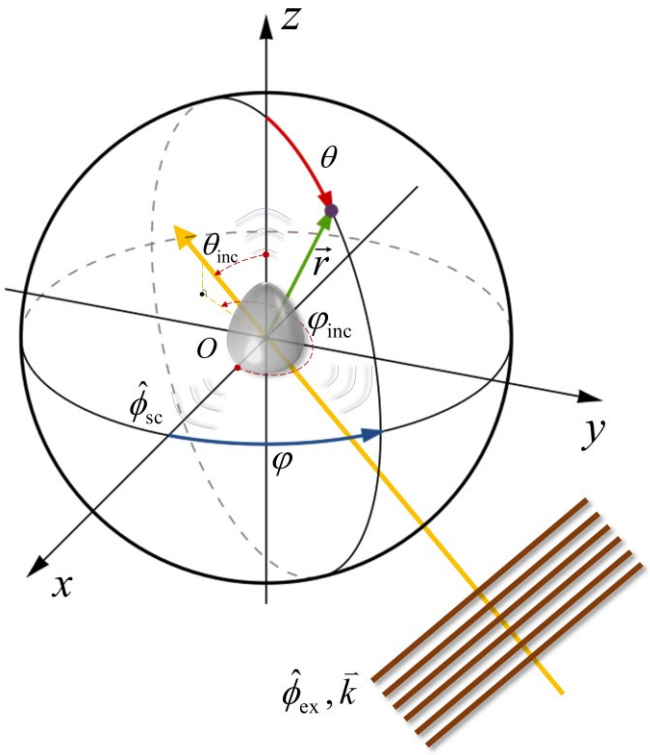

Figure 3: A diagram describing the interaction of an external plane wave with an axisymmetric body that is symmetric about the z-axis. The incidence angle of the external plane wave, $\hat{\phi}_{\mathrm{ex}}$, is described by its wave vector $\vec{k} = (k, \theta_{\mathrm{inc}}, \varphi_{\mathrm{inc}})$. The excited scattering potential from the irregular body is defined as $\hat{\phi}_{\mathrm{sc}}$ with respect to the coordinate systems O. A summation of the potential fields of the external and scattered waves for the same point gives the total potential amplitude at that position.

Consider a time-harmonic acoustic plane wave with arbitrary incidence interacting with an axisymmetric body, as shown in Fig. 3. The center of mass of the body defines

a coordinate system denoted as O, and the axis of symmetry of the body coincides with the z-axis (cf. Fig. 1). The acoustic velocity potential amplitude of the external incident wave at a specific position vector $\vec{r} = (r, \theta, \varphi)$ is $\hat{\phi}_{\text{ex}}(\vec{r})$ (denoted as $\hat{\phi}_{\text{ex}}$), with angular frequency ω propagating in a homogeneously inviscid fluid of density ρ_0 and adiabatic speed of sound c_{s}. The incident wave with a wavenumber of $k = \frac{\omega}{c_{\text{s}}}$ is characterized by the wave vector $\vec{k} = (k, \theta_{\text{inc}}, \varphi_{\text{inc}})$ where the polar and azimuthal angles $(\theta_{\text{inc}}, \varphi_{\text{inc}})$ give the wave propagating direction. In this case, the plane wave, $\hat{\phi}_{\text{ex}} = \text{e}^{\text{i}\vec{k}\vec{r}}$ (unit amplitude), can be formulated by a partial wave series as [35]

$$\hat{\phi}_{\text{ex}} = \sum_{n,m} a_{nm} J_n^m, \tag{7}$$

where the hat symbol $\hat{\cdot}$ represents the complex amplitude of the corresponding variable. Abbreviation $\sum_{n,m} \equiv \sum_{n=0}^{\infty} \sum_{m=-\infty}^{+\infty}$. The expansion coefficients of the partial wave series

$$a_{nm} = \text{i}^n 4\pi Y_n^m(\theta_{\text{inc}}, \varphi_{\text{inc}})^* \tag{8}$$

are also referred to as the external beam-shape coefficients. $Y_n^m(\theta_{\text{inc}}, \varphi_{\text{inc}})$ is the spherical harmonic function of n-th order and m-th degree determined by the incidence angle of the incident plane wave $(\theta_{\text{inc}}, \varphi_{\text{inc}})$. Abbreviation $J_n^m \equiv j_n(kr) Y_n^m(\theta, \varphi)$. $j_n(kr)$ is the spherical Bessel function of order n at a position r and $Y_n^m(\theta, \varphi)$ is the spherical harmonic function of n-th order and m-th degree at the angular position (θ, φ).

The total potential field $\hat{\phi}(\vec{r})$ (also denoted as $\hat{\phi}$) excited by the external wave at a specific position $\vec{r}$ with respect to the spherical coordinate system O satisfies the Helmholtz wave equation

$$(\nabla^2 + k^2)\hat{\phi} = 0, \tag{9}$$

where ∇^2 is the Laplacian operator. Physically, the total potential field is contributed by the external potential field $\hat{\phi}_{\text{ex}}$ and the scattering potential field reflected by the irregular body $\hat{\phi}_{\text{sc}}(\vec{r})$ (denoted as $\hat{\phi}_{\text{sc}}$)

$$\hat{\phi} = \hat{\phi}_{\text{ex}} + \hat{\phi}_{\text{sc}}. \tag{10}$$

The solution of the Helmholtz wave equation, Eq. (9), can be theoretically expressed by a partial wave series [35]. In order to keep consistent with the series expression of the external potential field, the velocity potential function for the scattered field by the spherical coordinate system O can be described as

$$\hat{\phi}_{\mathrm{sc}} = \sum_{n,m} s_{nm} a_{nm} H_n^m, \tag{11}$$

where the unknown scattering coefficients, s_{nm}, represent the scattering effects from the irregular body excited by the external plane wave. A combining function $H_n^m \equiv h_n(kr)Y_n^m(\theta,\varphi)$. $h_n(kr)$ is the Hankel function of the first kind at position r.

The conformal mapping transforms the Helmholtz wave equation (Eq. (9)) into [61]

$$\left(\nabla^2 + k^2 \Im(u,w)\right)\hat{\phi}(u,w,v) = 0, \tag{12}$$

where $\Im(u,w)$ is the Jacobian of the transformation from $(r_{\mathrm{s}}(\theta),\theta)$ system to (u,w) system. Evidently, if $\hat{\phi}$ is any solution of the Helmholtz equation, Eq. (9), in the spherical coordinate system, then $\hat{\phi}(u,w,v)$ is a solution of conformal mapping coordinate system, Eq. (12) [62]. Using the mapping relationships given in Eq. (2), the external and scattering potential fields on the new coordinate system can be expressed by transforming Eqs. (7) and (11)

$$\hat{\phi}_{\mathrm{ex}}(u,w,v) = \sum_{n,m} a_{nm} J_n^m(u,w,v), \tag{13}$$

and

$$\hat{\phi}_{\mathrm{sc}}(u,w,v) = \sum_{n,m} s_{nm} a_{nm} H_n^m(u,w,v), \tag{14}$$

where abbreviations $J_n^m(u,w,v) \equiv j_n\big(kr(u,w)\big)Y_n^m(\theta(u,w),v)$ and $H_n^m(u,w,v) \equiv h_n\big(kr(u,w)\big)Y_n^m(\theta(u,w),v)$. The quantities $r(u,w)$ and $\theta(u,w)$ can be determined by Eqs. (2) and (6). The summation of Eqs. (13) and (14) gives the total potential field in terms of the new coordinates (u,w,v), which also is the solution of Eq. (12).

In order to solve the unknown scattering coefficients s_{nm}, we need to apply the boundary condition on the interface between the irregular body and the host fluid ($u = u_0 = 0$).

2.3. Scattering coefficients of irregular bodies

To solve the potential field, the double infinite summations in Eqs. (13) and (14) must be truncated by a truncation number N, which limits the summations from $\sum_{n,m} \equiv \sum_{n=0}^{\infty} \sum_{m=-\infty}^{+\infty}$ to $\sum_{n,m} \equiv \sum_{n=0}^{N} \sum_{m=-N}^{N}$. It can be seen that the total number of unknown variables of the scattering coefficients s_{nm} in Eq. (14) includes $(N+1) \times (2N+1)$ system of equations is required to obtain the scattering coefficients s_{nm}.

For simplicity, the case of a sound-soft boundary will be discussed, but the issue is the same for the sound-hard case, which is derived in Appendix B. The Dirichlet boundary condition requires that the total potential vanishes on the surface of the scatterer $\hat{\phi}_{\mathrm{ex}}(u_0, w, v) + \hat{\phi}_{\mathrm{sc}}(u_0, w, v) = 0$ (derived from Eqs. (13) and (14)), which gives

$$\sum_{n,m} a_{nm} J_n^m(u_0, w, v) + \sum_{n,m} s_{nm} a_{nm} H_n^m(u_0, w, v) = 0. \tag{15}$$

The system of equations necessary to satisfy this boundary condition is generated by multiplying both sides of this equation by a set of spherical angular eigenfunctions [61]

$$\psi_{n'}^{m'}(w, v) = P_{n'}^{m'}\big(\cos(w)\big)\sin(w)\mathrm{e}^{-\mathrm{i}m'v} \tag{16}$$

and integrating over the range of w and v

$$\int_0^{\pi} \int_0^{2\pi} \left[\sum_{n,m} a_{nm} J_n^m(u_0, w, v) + \sum_{n,m} s_{nm} a_{nm} H_n^m(u_0, w, v) \right] \psi_{n'}^{m'}(w, v) \mathrm{d}v \mathrm{d}w = 0. \tag{17}$$

Considering the orthogonality relationship $\int_0^{2\pi} \mathrm{e}^{\mathrm{i}nw} \cdot \mathrm{e}^{-\mathrm{i}mw} \, \mathrm{d}w = 2\pi\delta_{n,m}$ and the definition of the spherical harmonic function $Y_n^m(\theta, \varphi) = \sqrt{\frac{(2n+1)}{4\pi} \cdot \frac{(n-m)!}{(n+m)!}} P_n^m\big(\cos(\theta)\big)\mathrm{e}^{\mathrm{i}m\varphi}$ [35], the above equation becomes

$$\sum_{n=0}^{N} a_{nm'} \Gamma_n^{n',m'} + \sum_{n=0}^{N} s_{nm'} a_{nm'} \Lambda_n^{n',m'} = 0, \quad (n' = 0,1,\cdots,N; m' = -N,\cdots,0,\cdots,N) \tag{18}$$

where the structural functions $\Gamma_n^{n',m'}$ and $\Lambda_n^{n',m'}$ are

$$\begin{cases} \Gamma_n^{n',m'} = \int_0^{\pi} [j_n\big(kr(u_0,w)\big)\sqrt{\dfrac{(2n+1)}{4\pi}\cdot\dfrac{(n-m)!}{(n+m)!}}P_n^{m'}\big(\cos\theta(u_0,w)\big) \\ \qquad\qquad P_{n'}^{m'}\big(\cos(w)\big)\sin(w)]\mathrm{d}w \\ \Lambda_n^{n',m'} = \int_0^{\pi} [h_n\big(kr(u_0,w)\big)\sqrt{\dfrac{(2n+1)}{4\pi}\cdot\dfrac{(n-m)!}{(n+m)!}}P_n^{m'}\big(\cos\theta(u_0,w)\big) \\ \qquad\qquad P_{n'}^{m'}\big(\cos(w)\big)\sin(w)]\mathrm{d}w \end{cases} . \tag{19}$$

Equation (18) immediately provides a set of $N+1$ equations for each fixed m' and totally a set of $(N+1)\times(2N+1)$ equations. Hence, by solving the system of linear equations, the scattering coefficients of the irregular body excited by a progressive plane wave are determined. A method to solve the system of equations is given in Appendix C.

2.4. Acoustic radiation force and torque

The acoustic radiation force on an object due to scattering phenomena was obtained as a surface integration R, which should involve the object [24][25]

$$\vec{F} = \int_{\mathrm{R}} \langle L\rangle \mathrm{d}\vec{A}_{\mathrm{R}} - \rho_0 \int_{\mathrm{R}} \mathrm{d}\vec{A}_{\mathrm{R}} \cdot \langle \vec{u}\vec{u}\rangle, \tag{20}$$

where the angle bracket $\langle\cdot\rangle$ denotes the time average of the variable therein. L is the acoustic Lagrange density defined as $L = \frac{1}{2}\rho_0\vec{u}\cdot\vec{u} - \frac{1}{2\rho_0 c_s^2}p^2$, where $\rho_0\vec{u}\cdot\vec{u}$ is the flux of momentum density. The acoustic velocity and the acoustic pressure are decomposed as $\vec{u} = \vec{u}_{\mathrm{ex}} + \vec{u}_{\mathrm{sc}}$ and $p = p_{\mathrm{ex}} + p_{\mathrm{sc}}$, respectively, with subscripts $\cdot_{\mathrm{ex}}$ and $\cdot_{\mathrm{sc}}$ for the external incident and scattered waves. The spherical surface R surrounding the scattering particle is sufficiently far to involve the scatterer, and the direction of the integration element $\mathrm{d}\vec{A}_{\mathrm{R}}$ is along the outer normal of the surface. Three factors are now considered: (i) for the external incident wave which does not contribute to the radiation force, i.e., $\int_{\mathrm{R}}\langle L_{\mathrm{ex}}\rangle \mathrm{d}\vec{A}_{\mathrm{R}} - \rho_0\int_{\mathrm{R}}\mathrm{d}\vec{A}_{\mathrm{R}}\cdot\langle\vec{u}_{\mathrm{ex}}\vec{u}_{\mathrm{ex}}\rangle = 0$, the acoustic Lagrange density for the incident wave is defined as $L_{\mathrm{ex}} = \frac{1}{2}\rho_0\vec{u}_{\mathrm{ex}}\cdot\vec{u}_{\mathrm{ex}} - \frac{1}{2\rho_0 c_s^2}p_{\mathrm{ex}}^2$; (ii) the Sommerfeld radiation condition requires the acoustic Lagrange density for the scattering wave to satisfy $L_{\mathrm{sc}} = \frac{1}{2}\rho_0\vec{u}_{\mathrm{sc}}\cdot\vec{u}_{\mathrm{sc}} - \frac{1}{2\rho_0 c_s^2}p_{\mathrm{sc}}^2 = 0$; and (iii) the pressure and

the particle velocity can be expressed by the potential field as $-\rho_0 \frac{\partial \phi}{\partial t} = p$ and $\nabla \phi = \vec{u}$. Equation (20) is reduced to

$$\vec{F} = \int_{\mathrm{R}} \frac{\rho_0 \omega^2}{c_{\mathrm{s}}^2} \left[\langle \phi_{\mathrm{ex}} \phi_{\mathrm{sc}} \rangle \vec{e}_r + \langle \phi_{\mathrm{sc}} \phi_{\mathrm{sc}} \rangle + \langle \frac{\mathrm{i} c_{\mathrm{s}}}{\omega} \phi_{\mathrm{sc}} \nabla \phi_{\mathrm{sc}} \rangle \right] \mathrm{d}\vec{A}_{\mathrm{R}}, \tag{21}$$

where $\vec{e}_r$ is the unit outer normal vector of the spherical surface R. The sum of terms makes two types of contributions, (i) squares of ϕ_{sc} representing the force from the scattered wave, and (ii) the mixed term meaning the force from interference between the incident and scattered waves.

Consequently, the acoustic radiation force on the irregular body can be evaluated under the Cartesian coordinate system by substituting Eqs. (7) and (11) into Eq. (21), using the relationship $\langle XY \rangle = \frac{1}{2} \mathrm{Re}\left(\hat{X}\hat{Y}^*\right)$. Considering the orthogonality and the recurrence properties of the spherical harmonics function [63] to simplify the expressions, we finally yield

$$\begin{aligned}
F_x = \frac{\rho_0}{4} \mathrm{Re}[\mathrm{i} \cdot \sum_{n,m} a_{nm}(1+s_{nm}) \big(& \mathcal{A}_{n+1}^{m+1} b_{n+1,m+1}^* \\
& - \mathcal{B}_{n-1}^{m+1} b_{n-1,m+1}^* + \mathcal{C}_{n+1}^{m-1} b_{n+1,m-1}^* - \mathcal{D}_{n-1}^{m-1} b_{n-1,m-1}^* \big)], \\
F_y = \frac{\rho_0}{4} \mathrm{Re}[\sum_{n,m} a_{nm}(1+s_{nm}) \big(& \mathcal{A}_{n+1}^{m+1} b_{n+1,m+1}^* \\
& - \mathcal{B}_{n-1}^{m+1} b_{n-1,m+1}^* - \mathcal{C}_{n+1}^{m-1} b_{n+1,m-1}^* + \mathcal{D}_{n-1}^{m-1} b_{n-1,m-1}^* \big)], \\
F_z = \frac{\rho_0}{2} \mathrm{Re}[\mathrm{i} \cdot \sum_{n,m} a_{nm}(1+s_{nm}) \big(& \mathcal{E}_{n+1}^{m} b_{n+1,m}^* \\
& - \mathcal{F}_{n-1}^{m} b_{n-1,m}^* \big)],
\end{aligned} \tag{22}$$

where abbreviation $b_{nm} = a_{nm} \cdot s_{nm}$ and symbol Re means taking the real part of the expression. The weighting coefficients $\mathcal{A}_n^m$, $\mathcal{B}_n^m$, $\mathcal{C}_n^m$, $\mathcal{D}_n^m$, $\mathcal{E}_n^m$, and $\mathcal{F}_n^m$ are given as

$$\mathcal{A}_n^m = -\sqrt{\frac{(n+m-1)(n+m)}{(2n-1)(2n+1)}}, \mathcal{B}_n^m = \sqrt{\frac{(n-m+2)(n-m+1)}{(2n+1)(2n+3)}},$$

$$\mathcal{C}_n^m = \sqrt{\frac{(n-m-1)(n-m)}{(2n-1)(2n+1)}}, \mathcal{D}_n^m = -\sqrt{\frac{(n+m+2)(n+m+1)}{(2n+1)(2n+3)}},$$

$$\mathcal{E}_n^m = \sqrt{\frac{(n-m)(n+m)}{(2n-1)(2n+1)}}, \mathcal{F}_n^m = -\sqrt{\frac{(n-m+1)(n+m+1)}{(2n+1)(2n+3)}}.$$

The acoustic radiation torque on an object have also been derived as a surface integration of the object [26]

$$\vec{T} = -\rho_0 \int_{\mathrm{R}} \langle \left(d\vec{A}_{\mathrm{R}} \cdot \vec{u} \right) \cdot (\vec{r} \times \vec{u}) \rangle. \tag{23}$$

Following relationships $-\rho_0 \frac{\partial \phi}{\partial t} = p$ and $\nabla \phi = \vec{u}$, the potential form of Eq. (23) is

$$\vec{T} = -\rho_0 \int_{\mathrm{R}} \langle \frac{\partial \phi}{\partial t} \cdot \mathrm{i}\vec{K}\phi \rangle \, dA_{\mathrm{R}}, \tag{24}$$

where $\vec{K} = -\mathrm{i}(\vec{r} \times \nabla)$ representing the angular momentum operator [63]. Similarly, we decompose the total potential field ϕ into the potential fields of external wave ϕ_{ex} and scattered wave ϕ_{sc} and eliminate the time-averaged effects using relationship $\langle XY \rangle = \frac{1}{2}\mathrm{Re}\left(\hat{X}\hat{Y}^*\right)$. The acoustic torque given in Eq. (24) becomes

$$\vec{T} = -\frac{\rho_0}{2}\mathrm{Re}\int_{\mathrm{R}} \left[\frac{\partial \hat{\phi}_{\mathrm{ex}}^*}{\partial r} \mathrm{i}\vec{K}\hat{\phi}_{\mathrm{sc}} - \hat{\phi}_{\mathrm{ex}}^* \mathrm{i}\vec{K} \frac{\partial \hat{\phi}_{\mathrm{sc}}}{\partial r} + \frac{\partial \hat{\phi}_{\mathrm{sc}}^*}{\partial r} \mathrm{i}\vec{K}\hat{\phi}_{\mathrm{sc}} \right] \mathrm{d}\vec{A}_{\mathrm{R}}. \tag{25}$$

By substituting Eqs. (7) and (11) into Eq. (25), with the help of relationships $(K_x \pm \mathrm{i}K_x)Y_n^m(\theta,\varphi) = \mathcal{G}_n^m Y_n^{m\pm1}(\theta,\varphi)$ and $K_z Y_n^m(\theta,\varphi) = mY_n^m(\theta,\varphi)$ [63] (K_x, K_y, and K_z are the Cartesian components of $\vec{K}$), the acoustic radiation torque on the irregular body can be formulated under the Cartesian coordinate system as

$$\begin{aligned} T_x &= \frac{\rho_0}{4k}\mathrm{Re}\sum_{n,m} a_{nm}(1+s_{nm})\left(\mathcal{G}_n^m b_{n,m+1}^* + \mathcal{G}_n^{-m} b_{n,m-1}^*\right) \\ T_y &= \frac{\rho_0}{4k}\mathrm{Im}\sum_{n,m} a_{nm}(1+s_{nm})\left(\mathcal{G}_n^m b_{n,m+1}^* - \mathcal{G}_n^{-m} b_{n,m-1}^*\right), \\ T_z &= \frac{\rho_0}{2k}\mathrm{Re}\sum_{n,m} a_{nm}(1+s_{nm}) m b_{n,m}^* \end{aligned} \tag{26}$$

where symbol Im means taking the imaginary part of the expression and the weighting coefficient $\mathcal{G}_n^m = \sqrt{(n-m)(n+m+1)}$.

In the limit of great distances from the scatterer (integrating surface R is far away from the scatterer), the new coordinate system becomes spherical, and therefore the scattering coefficients, s_{nm}, used in Eqs. (22) and (26) are acceptable by solving the system of equations in Eq. (18). Following Eqs. (22) and (26), the acoustic radiation force and torque on the axisymmetric irregular body can be evaluated. Finally, we would like to emphasize that the codes used to calculate the radiation force and torque are open-access in [64].

Note that both the theoretical and numerical models consider the inviscid approximation. Actually, fluids may support shear stress within the particle boundary layer, which may cause viscous effects on radiation force [65] and torque [66]. However, the inviscid method is approximately correct for manipulated objects significantly larger than the thickness of the acoustic boundary layer [67][68]

$$\delta = \sqrt{\frac{2\mu_0}{\rho_0 \omega}}, \tag{27}$$

where μ_0 is the dynamic viscosity of the fluid. In our interests, the driving frequencies range from 2 MHz to 8 MHz, and the boundary layer widths vary from 0.4 μm to 0.2 μm in water at room temperature, which is much smaller than the average radius of the manipulated objects used in this work ($a = 50$ μm, referred to Tab. 3). Hence, the viscous contributions on the acoustic radiation force and torque can be discarded.

3. Results and discussion

3.1. Truncation number

We need to impose a truncation number of partial wave series, N, in the number of modes entering the computations of acoustic radiation force in Eq. (22) and acoustic radiation torque in Eq. (26). In this paper, the truncation number N is determined using a coefficient-ratio condition

$$q = \max_{(n = 1,2,\cdots,10)} \left| \frac{s_{N+n,0}}{s_{N,0}} \right| \leq 0.01 \,. \tag{28}$$

We increase the truncation number N until the ratio q is smaller than 0.01 to save computational time by ignoring the diminishing contributions in the series [45]. In Tab. 2, we list the ratio values and computational time for different N and find $N \geq 10$ to be satisfactory, while the patrial wave series is truncated as $N = 10$ in subsequent studies.

Table 2: Convergence analysis using coefficient-ratio, q, in different truncation numbers and various irregular bodies. In all cases, the size parameter $ka = 1.68$.

	$N = 8$	$N = 9$	$N = 10$	$N = 11$	$N = 12$
Ellipsoid	0.78 %	0.67 %	0.59 %	0.52 %	0.48 %
Cone	1.16 %	0.97 %	0.83 %	0.67 %	0.44 %
Diamond	1.29 %	1.07 %	0.92 %	0.73 %	0.71 %
CPU Time	~ 4.5 s	~ 6.0 s	~ 7.9 s	~ 9.5 s	~ 13.5 s

3.2. Validation and discussion

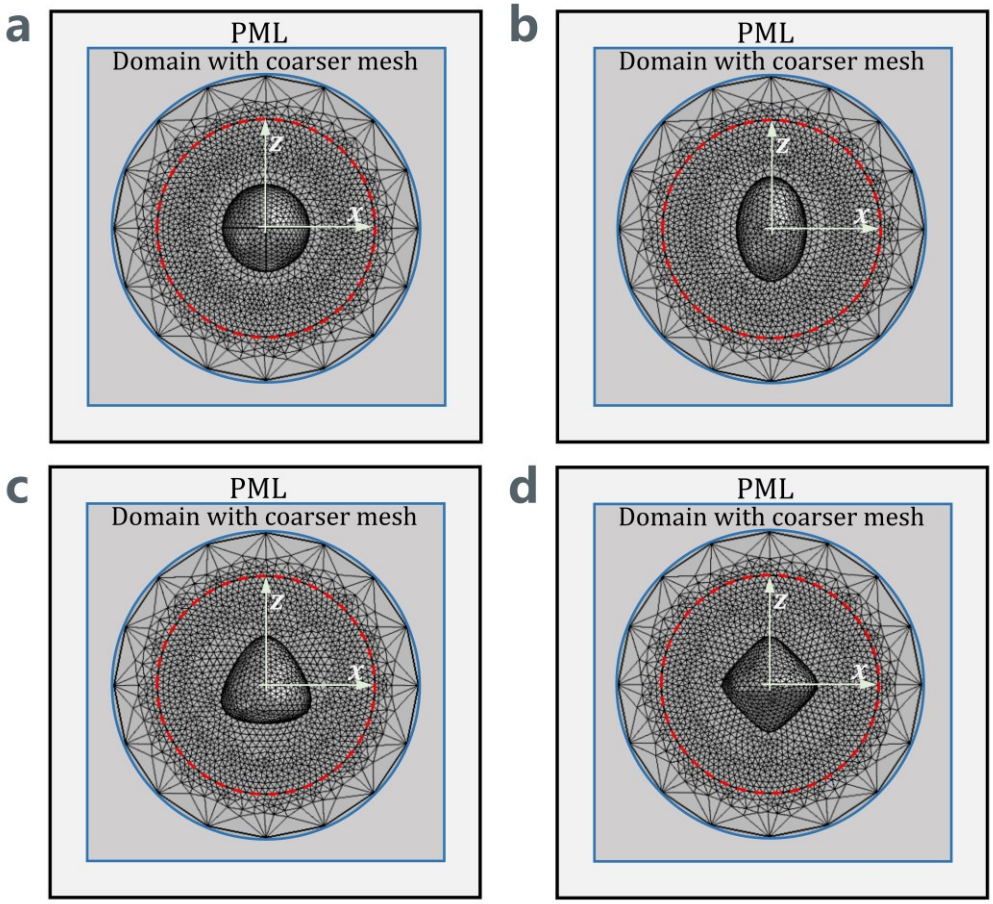

Figure 4: Sketch of the finite-element mesh used to compute the acoustic radiation force and torque on various bodies of **a)** sphere, **b)** ellipsoid, **c)** cone, and **d)** diamond. The numerical model comprises a cubic region as the simulation domain surrounding by a layer of acoustic perfectly matched layer (PML) with the thickness of $\lambda/2$. The center of mass of the irregular bodies is placed at the origin of the simulation domain. The simulation domain is divided into two sub-domains by the light blud surface (radius of $3.5a$). A finer mesh (maximum element size is $\lambda/65$) with $\sim 4.5 \times 10^5$ elements is defined inside the volume enclosed by the light blue surface. Outside this region, a coarser mesh (maximum element size is $\lambda/6$) is used with $\sim 0.8 \times 10^5$ elements. The red-dashed surface (radius of $2.5a$) depicts the integration control surface R, placed inside the domain with finer mesh to increase the numerical accuracy of the integrations.

We have performed a set of finite-element simulations of the wave-body interaction

in water to validate the acoustic radiation force and torque as prescribed in Eqs. (22) and (26). The full three-dimensional simulations are established in COMSOL Multiphysics 5.5 (COMSOL). The geometric settings are described as follows. A cubic region ($30a \times 30a \times 30a$) is defined as the simulation domain. The center of mass of the irregular bodies and the center of the simulation domain are both placed at the origin of the Cartesian coordinate system. A spherical surface with a radius of $3.5a$ (marked by light blue circles in Fig. 4) is defined to divide the whole simulation domain into two sub-domains, a finer mesh domain and a coarser mesh domain inside and outside the surface, respectively. We set another spherical surface R (marked by red-dashed circles in Fig. 4) with a radius of $2.5a$ inside the finer mesh domain as the integration surface to compute the numerical radiation force and torque as prescribed in Eqs. (20) and (23). A detailed numerical scheme in computing Eqs. (20) and (23) under the Cartesian coordinate system is given in Appendix D. The cross-sectional sketch (xz-plane) of the finite-element model and mesh distribution inside the finer mesh domain is displayed in Fig. 4.

The sound-soft boundary condition for the irregular bodies is applied in the numerical simulations, corresponding to the scattering coefficients solving in Eq. (18) used in evaluating the radiation force and torque by our method. Note that the scattering coefficients for the sound-hard boundary condition can be found in Appendix B. The Sommerfeld radiation condition is required to eliminate the acoustic Lagrange density of scattering waves in yielding Eq. (22), which is achieved by applying the perfect matched layer (PML) surrounding the simulation domain. The incident plane wave with unit pressure amplitude is set in COMSOL as a "background pressure field". To verify the correctness of the numerical integrations for the radiation force and torque, we have performed a mesh convergence analysis by gradually increasing the mesh density inside the finer mesh domain. It is found that when the maximum element size inside the finer mesh domain is $\lambda/65$ (as illustrated in Fig. 4), the evaluated radiation force and torque become less sensitive (vary within 1.0 %) with further increase of the mesh density. Following the above considerations, we summarize the simulational parameters in Tab. 3. It is worth mentioning that the computational time of each numerical simulation will take about 10 minutes, which is much higher than the time cost in our method (seeing Tab. 2).

Table 3: General parameters used in the finite-element simulations in COMSOL at room temperature and pressure. Note that the geometry of different irregular bodies is formulated in Eq. (2), where the mapping functions and mapping coefficients are given in Eq. (6) and Tab. 1, respectively.

Parameter	*Value*
Average radius of bodies (a)	50 μm
Density (water ρ_0)	1000 kg/m^3
Speed of sound (water c_s)	1500 m/s
Pressure peak (p_0)	1 Pa
Incidence polar angle (θ_{inc})	$0,\ \pi/6,\ \pi/3,\ \pi/2$ rad
Frequency of external wave (f_0)	2, 3, 4, 5, 6, 7 MHz
Size parameter (ka)	0.4, 0.6, 0.8, 1.1, 1.3, 1.5
Wavelength (λ)	c_s / f_0
Cubic simulational domain	$30a \times 30a \times 30a$
Radius of integrating surface R	$2.5a$
Radius of finer mesh domain	$3.5a$
Maximum element size (finer mesh domain)	λ / 65
Maximum element size (coarser mesh domain)	λ / 6
PML depth	λ / 2
CPU	Intel i7-6700HQ 2.6 GHz
Operating system	Windows 10
Maximum memory usage	~ 16 GB
Computational time per case	~ 10 min

To compare the obtained numerical results with theory, we use the normalized root-mean-square error (NRMSE),

$$\begin{cases} Err_{\mathrm{F},i} = \sqrt{\frac{1}{M}\sum_{m=1}^{M}\left(\tilde{Y}_{i,m} - \bar{Y}_{i,m}\right)^2} \\ Err_{\mathrm{T},i} = \sqrt{\frac{1}{M}\sum_{m=1}^{M}\left(\tilde{D}_{i,m} - \bar{D}_{i,m}\right)^2} \end{cases}, \tag{29}$$

where M is the number of sampling points (referred to the parameters listed in Tab. 3, $M = 24$ for frequencies ranging from 2 to 7 MHz with the interval of 1 MHz, while the incident polar angles are set to $0, \pi/6, \pi/3, \pi/2$ rad). The errors for the acoustic

radiation force and torque along the i-th direction ($i = x, y, z$) are denoted by $Err_{\mathrm{F},i}$ and $Err_{\mathrm{T},i}$, respectively. $Y_{i,m} = \frac{[F_{i,m} - \min(F_{i,m})]}{[\max(F_{i,m}) - \min(F_{i,m})]}$ and $D_{i,m} = \frac{[T_{i,m} - \min(T_{i,m})]}{[\max(T_{i,m}) - \min(T_{i,m})]}$ with a bar-hat mean, respectively, the normalized acoustic radiation force and torque on the i-th axis evaluated by numerical simulations, while those with a tilde-hat are the corresponding normalized results based on theoretical calculations.

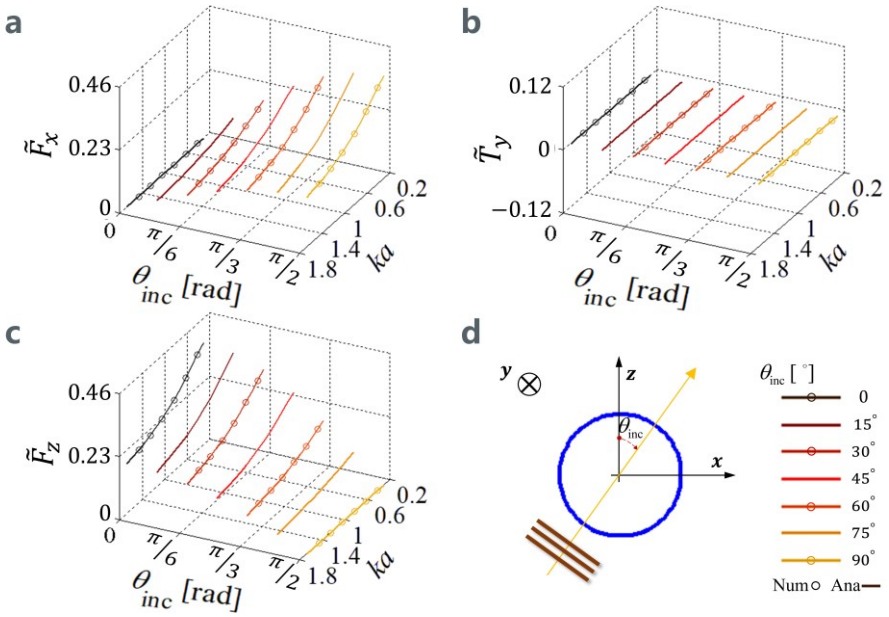

Figure 5: Theoretical and numerical calculations of the acoustic radiation force efficiencies, $\tilde{F}_x = F_x/[(\pi a^2 p_0)/(2\rho_0 c_0^2)]$ and $\tilde{F}_z = F_z/[(\pi a^2 p_0)/(2\rho_0 c_0^2)]$, and torque efficiency, $\tilde{T}_y = T_y/[(\pi a^3 p_0)/(2\rho_0 c_0^2)]$, resulting from an incident plane wave ($\hat{p} = 1$ Pa) acting on a soft spherical body (average radius of $a = 50$ μm) as a function of the polar angle of the incident wave, θ_{inc}, and the scaled size parameters, ka. Sub-figures **a)** and **c)** display the plots for the acoustic radiation force efficiencies along, respectively, x- and z- axes, while sub-figure **b)** displays the acoustic radiation torque efficiency along the y-axis. The circle markers represent the results based on the full three-dimensional numerical simulations, and the solid lines are derived from the theoretical calculations. The polar angle of incident wave ranges from 0° or $+z$-axis (black lines and circles) to 90° or $+x$-axis (orange lines and circles). Sub-figure **d)** illustrates an incident plane wave with arbitrary polar angles interacting with a spherical body under the Cartesian coordinate system. The center of mass of the spherical body coincides with the origin of the Cartesian coordinate system.

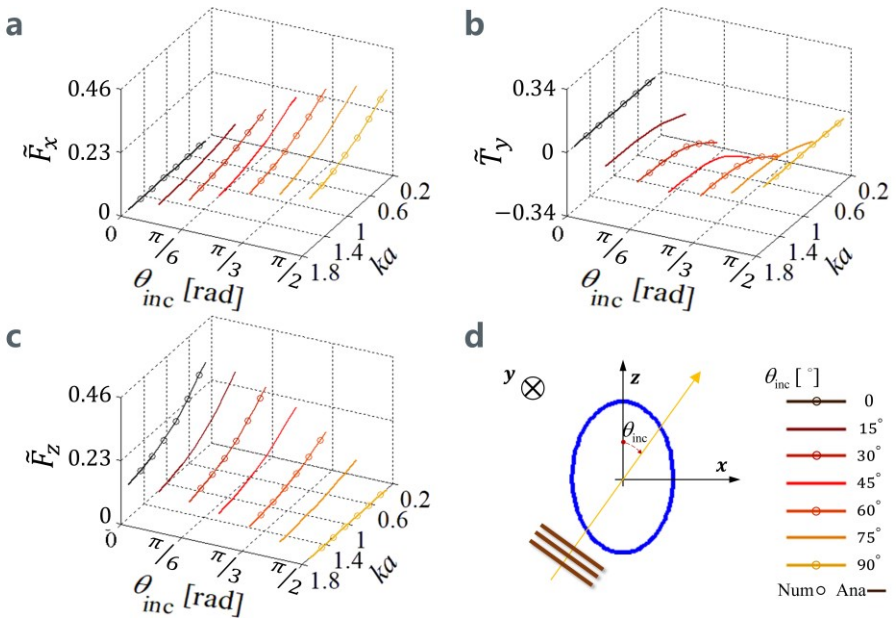

Figure 6: The same as in Fig. 5, but replaced the spherical body with ellipsoid (depicted in the lower-left corner of Fig. 2**b**). Note that the scale range for the acoustic radiation torque efficiency in sub-figure **b)** is replaced with $[-0.34,0.34]$ to better illustrate the results.

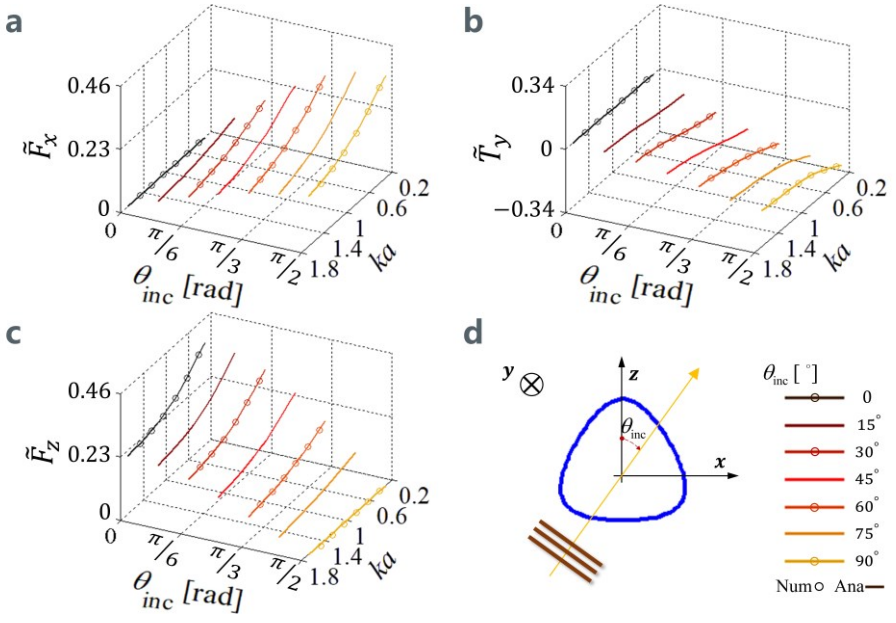

Figure 7: The same as in Fig. 5, but replaced the spherical body with cone (depicted in the lower-left corner of Fig. 2**c**). Note that the scale range for the acoustic radiation torque efficiency in sub-figure **b)** is replaced with $[-0.34,0.34]$ to better illustrate the results.

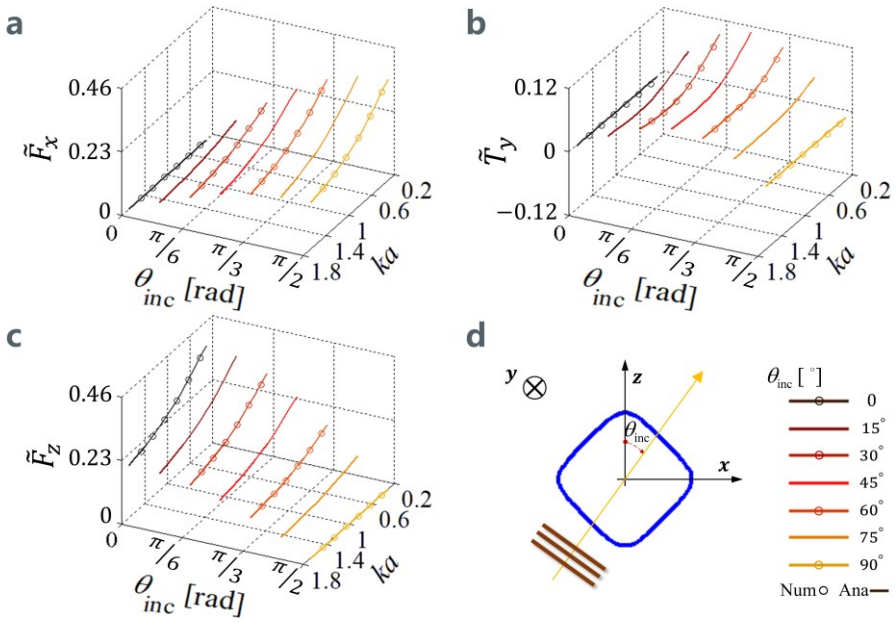

Figure 8: The same as in Fig. 5, but replaced the spherical body with diamond (depicted in the lower-left corner of Fig. 2**d**).

Table 4: The normalized root-mean-square error (NRMSE) of the acoustic radiation force and torque compared with numerical results, defined in Eq. (29)

		$i = x$	$i = y$	$i = z$
Sphere	$Err_{\mathrm{F},i}$ [%]	2.15	5.56	5.02
	$Err_{\mathrm{T},i}$ [%]	< 0.01	< 0.01	< 0.01
Ellipsoid	$Err_{\mathrm{F},i}$ [%]	1.66	5.16	4.45
	$Err_{\mathrm{T},i}$ [%]	< 0.01	2.55	< 0.01
Cone	$Err_{\mathrm{F},i}$ [%]	2.19	5.55	5.12
	$Err_{\mathrm{T},i}$ [%]	0.03	2.76	0.02
Diamond	$Err_{\mathrm{F},i}$ [%]	2.18	4.64	5.00
	$Err_{\mathrm{T},i}$ [%]	0.06	1.04	0.03

The theoretical evaluations of the acoustic radiation force and torque using Eqs. (22) and (26) compared with those calculations from full numerical simulations using Eqs. (20) and (23) (referred to Eqs. (D.2) and (D.3) in Appendix D for the specific numerical schemes) on various irregular geometries. Consider that the values computed for the radiation force, $F_i, (i = x, y, z)$, and torque, $T_i, (i = x, y, z)$, are extremely small, we dimensionless the radiation force and torque. Specifically, the dimensionless

radiation force efficiency is scaled as $\tilde{F}_i = F_i/[(\pi a^2 p_0)/(2\rho_0 c_0^2)]$, and the dimensionless radiation torque efficiency is $\tilde{T}_i = T_i/[(\pi a^3 p_0)/(2\rho_0 c_0^2)]$ as shown in Figs. 5 to 9. Considering the axisymmetric physics, we set the azimuthal angle of the incident plane wave as $\varphi_{\text{inc}} = 0$, which means the plane wave is propagated on the xz-plane. Consequently, the acoustic radiation force along y-axis, F_y, and the acoustic radiation torque along x- and z-axes, T_x and T_z, are significantly weaker than the corresponding values on other sensitive directions, i.e., $F_x \sim F_z \gg F_y \sim 0$ and $T_y \gg T_x \sim T_y \sim 0$. Therefore, we only plot and discuss the acoustic radiation force efficiencies along x- and z-axes, $\tilde{F}_x$ and $\tilde{F}_z$, as well as the acoustic radiation torque efficiency along y-axis, $\tilde{T}_y$, resulting from the incident plane wave with different frequencies and polar angles interacting with the irregular bodies. However, the NRMSEs of all x, y, and z components of the acoustic radiation force and torque compared the theoretical evaluations with the numerical results based on Eq. (29) are listed in Tab. 4. Both visual inspections and NRMSEs indicate an excellent agreement of acoustic radiation force and torque between our method and the full numerical simulations, while our formulations cost a shorter computational time than those based on the full finite-element method.

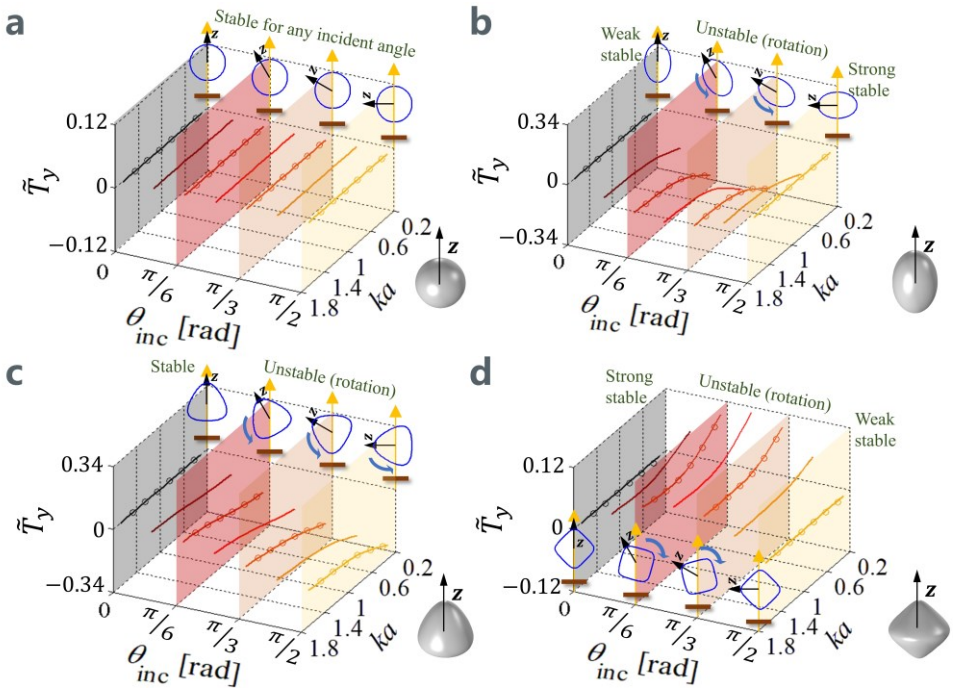

Figure 9: The stable positions of **a)** sphere, **b)** ellipsoid, **c)** cone, and **d)** diamond under the acoustic radiation torque excited by a traveling plane wave. The definition

of the polar angle, θ_{inc}, of the incident wave as well as the Cartesian coordinate system are the same as those described in Figs. 5 to 8. The radiation torque will rotate the manipulated body (under unstable conditions) until the body remains stable in its corresponding (strong) stable state.

For the same value of the average radius of different bodies ($a = 50$ μm), the acoustic radiation forces illustrated in sub-figures **a** and **c** of Figs. 5, 6, 7, and 8 are basically identical, indicated that the radiation force is not heavily affected by the differences of scatterer geometries. Additionally, with size parameter ka (i.e., frequency f_0) increases and for the same incident polar angle θ_{inc}, the radiation forces decrease monotonically before leveling off after $ka > 1.5$, meaning that the more acquirable low-frequency wave field provides higher efficiency in manipulating soft objects. As the polar angle θ_{inc} increases, $\tilde{F}_x$ increases. The exact opposite situation is encountered for the z-component, $\tilde{F}_z$. For $\theta_{\mathrm{inc}} = 0$ or $\pi/2$, $\tilde{F}_x$ or $\tilde{F}_z$ vanishes as required by symmetry. By contrast, as can be found in sub-figure **b** of Figs. 5, 6, 7, and 8, the acoustic radiation torques are strongly dependent on the shape of the irregular bodies. For the sphere (Fig. 5**b**), the radiation torque $\tilde{T}_y$ vanishes as required by symmetry. In different size parameters ka (i.e., frequencies f_0) and incidence θ_{inc}, for the ellipsoid and cone (Figs. 6**b** and 7**b**), the radiation torques $\tilde{T}_y$ are negative, meaning that the sense of rotation is in the counter-clockwise direction under xz-plane, whereas for diamond (Fig. 8**b**), the radiation torque $\tilde{T}_y$ reverses sign, meaning that the sense of rotation is in the clockwise direction. Furthermore, the radiation torque reaches a maximum (in the absolute sense) at $\theta_{\mathrm{inc}} \approx \pi/4$ for ellipsoid and diamond. The difference is that for the cone, the radiation torque increases as θ_{inc} increases and maximum efficiency is obtained at $\theta_{\mathrm{inc}} \approx \pi/2$. It can be seen from Fig. 9 that the radiation torque prefers to rotate the irregular bodies and finally stabilizes them in strong stable positions (a slight deviation of the incident angle will disrupt the balance of the body in a weak stable position). Consequently, the symmetry axis of the body is consistent or orthogonal to the propagation direction of the incident wave. This feature allows us to rotate the irregular bodies by adjusting the incident wave fields.

4. Concluding remarks

We have presented an explicit analytical method to compute the acoustic radiation force and torque acting on various axisymmetric, irregular bodies excited by a plane traveling wave with arbitrary incidences in the inviscid fluid based on conformal mapping procedure and partial wave series expansion. Two mapping functions and a set of mapping coefficients (referred to Appendix A and Tab. 1) were introduced to conformally map the variables to a new orthogonal coordinate system, where the irregular surface can be exactly described by the new radial coordinate as $u = u_0 = 0$ (i.e., a spherical surface in the new coordinate system). As a result, the boundary conditions on the surface are much more easily to enforce, and remain intact after the transformation due to the angle-preserving nature. The closed-form scattering expansion coefficients used to specify the scattering field were obtained by solving a set of the system of equations (referred to Appendix C), which is designed to eliminate the angular coordinates and satisfy the boundary conditions by multiplying a set of spherical angular eigenfunctions and integrating over the definition of angular coordinates. Then, the asymptotic radiation force and torque could be attained based on the solved scattering expansion coefficients.

Here, acoustic radiation force and torque exerted, respectively, on a sphere, an ellipsoid, a cone, and a diamond with sound-soft boundary condition (and sound-hard boundary condition is derived in Appendix B) suspended in water were calculated and analyzed. Validations of the analytical solution (seeing Figs. 5 to 8) were conducted through comparisons of the current results with the full three-dimensional numerical solutions (the numerical scheme is given in Appendix D). It could be found that the analytical method requires much less computational time (~ 7.9 s by common personal computers, Tab. 2) without loss of accuracy (NRMSEs $\leq$ 5.0 %, Tab. 4). Furthermore, the radiation force tendencies reveal that the radiation force is basically identical regardless of the differences in geometry. Consequently, it is acceptable for the wave-driven methods to neglect the geometric differences of objects in transportation. By contrast, the radiation torque is closely related to the cross-sectional shape of irregular bodies. It is apt to rotate the axisymmetric body so that the axis of symmetry is consistent with or orthogonal to the propagation direction of the incident wave (seeing

Fig. 9), which provides theoretical guidance for the use of the acoustic wave fields to rotate specific irregular geometries.

We propose an effective and efficient method to predict the motion of various irregular objects, which helps to understand the behavior of the irregular bodies over a wide range of size parameters in the acoustic wave fields.

Appendix A: Determination of mapping coefficients

A method to determine the mapping coefficients can be found in work [59], here we have given as below. On the boundary of the slice of the irregular body, we equating $r_s(\theta)\mathrm{e}^{\mathrm{i}\theta}$ in Eq. (5) to complex mapping function $M(u,w)$ in Eq. (6) with $u = u_0$=0 yields

$$a\mathrm{e}^{\mathrm{i}\theta} + \sum_{n=1}^{\infty}\left[R_n^*\mathrm{e}^{\mathrm{i}(1+n)\theta} + R_n\mathrm{e}^{\mathrm{i}(1-n)\theta}\right] = c_{-1}\mathrm{e}^{\mathrm{i}w} + \sum_{n=0}^{\infty} c_n\mathrm{e}^{-\mathrm{i}nw}\,. \tag{A.1}$$

Since the boundary of the slice is a periodic function, the deviation of θ from w can be represented as a Fourier series

$$\theta = w + \sum_{n=1}^{\infty}[E_n\cos(nw) + F_n\sin(nw)]. \tag{A.2}$$

In the above equation, the series coefficients E_n and F_n are unknown, while can be determined by orthogonality relationship of complex exponential functions $\int_0^{2\pi}\mathrm{e}^{\mathrm{i}nw}\cdot\mathrm{e}^{-\mathrm{i}mw}\,\mathrm{d}w = 2\pi\delta_{n,m}$, where $\delta_{n,m}$ is the Kronecker delta function. We multiply both sides of Eq. (A.1) by $\frac{1}{2\pi}\mathrm{e}^{-\mathrm{i}mw}$ and integrating over w from 0 to 2π

$$\begin{cases}\dfrac{1}{2\pi}\displaystyle\int_0^{2\pi}\mathrm{e}^{-\mathrm{i}mw}\left\{a\mathrm{e}^{\mathrm{i}\theta} + \sum_{n=1}^{\infty}\left[R_n^*\mathrm{e}^{\mathrm{i}(1+n)\theta} + R_n\mathrm{e}^{\mathrm{i}(1-n)\theta}\right]\right\}\mathrm{d}w = 0, \quad m > 1 \\ \dfrac{1}{2\pi}\displaystyle\int_0^{2\pi}\mathrm{e}^{-\mathrm{i}mw}\left\{a\mathrm{e}^{\mathrm{i}\theta} + \sum_{n=1}^{\infty}\left[R_n^*\mathrm{e}^{\mathrm{i}(1+n)\theta} + R_n e^{\mathrm{i}(1-n)\theta}\right]\right\}\mathrm{d}w = c_{-m},\ m \le 1\end{cases}. \tag{A.3}$$

Based on Eq. (A.3), the series coefficients E_n and F_n can be solved using the upper equation, which are then used to obtain the mapping coefficients through the lower equation.

Appendix B: Neumann boundary condition

Based on the mapping relationships given in Eq. (1), the position vector can be generally expressed as

$$\vec{r} = f(u,w)\cdot\cos(v)\vec{e}_x + f(u,w)\cdot\sin(v)\vec{e}_y + g(u,w)\vec{e}_z \tag{B.1}$$

where $\vec{e}_x$, $\vec{e}_y$, and $\vec{e}_z$ are unit vectors along the corresponding coordinate axes. In the new coordinate system, the orthogonal coordinate system is desirable since it facilitates the computation of the normal particle velocity on the boundary. Orthogonality of the new coordinate system requires that the partial derivative of the position vector $\vec{r}$ in

Eq. (B.1) satisfies

$$\vec{r}_u \cdot \vec{r}_w = 0;\ \vec{r}_u \cdot \vec{r}_v = 0;\ \vec{r}_v \cdot \vec{r}_w = 0, \tag{B.2}$$

where the subscripts mean the partial derivative of corresponding variables. Considering the mapping relationship given in Eq. (B.1), the partial derivatives of the position vector with respect to each of the variables are

$$\begin{cases} \vec{r}_u = f_u(u,w)\cdot\cos(v)\vec{e}_x + f_u(u,w)\cdot\sin(v)\vec{e}_y + g_u(u,w)\vec{e}_z \\ \vec{r}_w = f_w(u,w)\cdot\cos(v)\vec{e}_x + f_w(u,w)\cdot\sin(v)\vec{e}_y + g_w(u,w)\vec{e}_z \\ \vec{r}_v = -f(u,w)\cdot\sin(v)\vec{e}_x + f(u,w)\cdot\cos(v)\vec{e}_y \end{cases}, \tag{B.3}$$

Inserting Eq. (B.3) into Eq. (B.2), it can prove that the new coordinate system could be orthogonal if the mapping functions satisfy

$$f_u(u,w) = g_w(u,w) \ \text{ or } \ f_w(u,w) = g_u(u,w)\,. \tag{B.4}$$

The Neumann boundary condition requires that the normal particle velocity vanishes on the scatterer surface $\vec{n}\cdot\nabla\left[\hat{\phi}_{\text{ex}}(u_0,w,v) + \hat{\phi}_{\text{sc}}(u_0,w,v)\right] = 0$, where $\vec{n}$ is the outer normal vector to the surface. It can be found that the mapping functions given in Eq. (6) satisfy the orthogonal requirements in Eq. (B.4). Consequently, the gradient of the potential field is

$$\nabla\hat{\phi}(u_0,w,v) = \frac{\partial\hat{\phi}(u_0,w,v)}{\partial u}\frac{\vec{r}_u}{r_u} + \frac{\partial\hat{\phi}(u_0,w,v)}{\partial w}\frac{\vec{r}_w}{r_w} + \frac{\partial\hat{\phi}(u_0,w,v)}{\partial v}\frac{\vec{r}_v}{r_v} \tag{B.5}$$

where vectors $\vec{r}_u$, $\vec{r}_w$ and $\vec{r}_v$ are given in Eq. (B.3). As the scatterer surface has been defined by $u = u_0 = 0$, the outer normal vector $\vec{n}$ is parallel to $\vec{r}_u$. Hence, the Neumann boundary condition becomes

$$\frac{1}{\sqrt{f_u^2 + f_w^2}}\frac{\partial\left[\hat{\phi}_{\text{ex}}(u_0,w,v) + \hat{\phi}_{\text{sc}}(u_0,w,v)\right]}{\partial u} = 0 \tag{B.6}$$

Inserting Eqs. (13) and (14) into the above equation, multiplying both sides by the spherical angular eigenfunctions and considering the orthogonality relationship $\int_0^{2\pi} \mathrm{e}^{\mathrm{i}nw}\cdot\mathrm{e}^{-\mathrm{i}mw}\,\mathrm{d}w = 2\pi\delta_{n,m}$, we finally yield

$$\sum_{n=0}^{N} a_{nm'}\Gamma_{n,u}^{n',m'} + \sum_{n=0}^{N} s_{nm'}a_{nm'}\Lambda_{n,u}^{n',m'} = 0, \quad (n' = 0,1,\cdots,N;\ m' = -N,\cdots,0,\cdots,N) \tag{B.7}$$

where $\Gamma_{n,u}^{n',m'}$ and $\Lambda_{n,u}^{n',m'}$ are the partial derivative of the new radial coordinate of structural functions $\Gamma_n^{n',m'}$ and $\Lambda_n^{n',m'}$ given in Eq. (19):

$$\begin{cases} \Gamma_{n,u}^{n',m'} = \left.\dfrac{\partial \Gamma_n^{n',m'}}{\partial u}\right|_{u=u_0} \\ \Lambda_{n,u}^{n',m'} = \left.\dfrac{\partial \Lambda_n^{n',m'}}{\partial u}\right|_{u=u_0} \end{cases}. \tag{B.8}$$

Appendix C: Solution of the system of equations

Based on Eq. (18), for each combination of (n', m'), we can obtain an additional equation to close the system. There are totally $(N+1)\times(2N+1)$ additional equations and $(N+1)\times(2N+1)$ unknown scattering coefficients $s_{n'm'}$. For a fixed index of m', the change of index of $n' = 0,1,\cdots,N$ is able to provide $N+1$ additional equations as

$$\begin{bmatrix} a_{0m'}\Lambda_0^{0,m'} & a_{1m'}\Lambda_1^{0,m'} & \cdots & a_{Nm'}\Lambda_N^{0,m'} \\ a_{0m'}\Lambda_0^{1,m'} & a_{1m'}\Lambda_1^{1,m'} & \cdots & a_{Nm'}\Lambda_N^{1,m'} \\ \vdots & \vdots & \ddots & \vdots \\ a_{0m'}\Lambda_0^{N,m'} & a_{1m'}\Lambda_1^{N,m'} & \cdots & a_{Nm'}\Lambda_N^{N,m'} \end{bmatrix} \cdot \begin{bmatrix} s_{0m'} \\ s_{1m'} \\ \vdots \\ s_{Nm'} \end{bmatrix} = \begin{bmatrix} \mathrm{A}^{0,m'} \\ \mathrm{A}^{1,m'} \\ \vdots \\ \mathrm{A}^{N,m'} \end{bmatrix} \tag{C.1}$$

where abbreviation $\mathrm{A}^{n',m'} = \sum_{n=0}^{N} a_{nm'}\Gamma_n^{n',m'}$. Solving the above linear equations can get $N+1$ scattering coefficients $s_{n'm'}$ $(n' = 0,1,\cdots,N)$. The change of index of m' from $-N$ to N gives a total of $2N+1$ linear systems, and therefore all the unknown scattering coefficients $s_{n'm'}$ $(n' = 0,1,\cdots,N; m' = -N,\cdots,0,\cdots,N)$ can be determined by solving $2N+1$ linear systems, corresponding to different index of m'.

Appendix D: Numerical evaluation of radiation force and torque

The outer normal vector of integrating surface R can be expressed as $\mathrm{d}\vec{A}_\mathrm{R} = \vec{e}_\mathrm{R}\mathrm{d}A_\mathrm{R}$, where $\vec{e}_\mathrm{R} = \left(\frac{x}{a_\mathrm{R}}, \frac{y}{a_\mathrm{R}}, \frac{z}{a_\mathrm{R}}\right)$ defined as the unit outer normal vector of spherical surface R with a radius of $a_\mathrm{R} = \sqrt{x^2+y^2+z^2}$. The point position on the integrating surface is denoted as (x, y, z) under the Cartesian coordinate system. Inserting $\mathrm{d}\vec{A}_\mathrm{R} = \vec{e}_\mathrm{R}\mathrm{d}A_\mathrm{R}$ into Eqs. (20) and (23), using a tensor relation $\vec{e}_\mathrm{R}\cdot(\vec{u}\vec{u}) = (\vec{e}_\mathrm{R}\cdot\vec{u})\vec{u}$, we arrive at

$$\begin{cases} \vec{F} = \int_{\mathrm{R}} \langle \frac{\rho_0}{2} \vec{u} \cdot \vec{u} - \frac{1}{2\rho_0 c_s^2} p^2 \rangle \, \vec{e}_{\mathrm{R}} \mathrm{d}A_{\mathrm{R}} - \rho_0 \int_{\mathrm{R}} \langle (\vec{e}_{\mathrm{R}} \cdot \vec{u}) \vec{u} \rangle \mathrm{d}A_{\mathrm{R}} \\ \vec{T} = -\rho_0 \int_{\mathrm{R}} \langle (\vec{e}_{\mathrm{R}} \cdot \vec{u}) \cdot (\vec{r} \times \vec{u}) \rangle \mathrm{d}A_{\mathrm{R}} \end{cases} . \tag{D.1}$$

Using the relationship $\langle XY \rangle = \frac{1}{2} \mathrm{Re}\left(\hat{X}\hat{Y}^*\right)$, the radiation force and torque are rearranged along corresponding coordinate axes under the Cartesian coordinate system as

$$\begin{aligned} F_x = \vec{F} \cdot \vec{e}_x &= \int_{\mathrm{R}} \frac{1}{4} \frac{x}{a_{\mathrm{R}}} \left[\rho_0 \mathrm{Re}\left(\hat{\vec{u}} \cdot \hat{\vec{u}}^*\right) - \frac{1}{\rho_0 c_s^2} \mathrm{Re}(\hat{p} \cdot \hat{p}^*) \right] \mathrm{d}A_{\mathrm{R}} \\ &\quad - \frac{\rho_0}{2} \int_{\mathrm{R}} \left[\frac{x}{a_{\mathrm{R}}} \mathrm{Re}(\hat{u}_x \cdot \hat{u}_x^*) + \frac{y}{a_{\mathrm{R}}} \mathrm{Re}\left(\hat{u}_x \cdot \hat{u}_y^*\right) + \frac{z}{a_{\mathrm{R}}} \mathrm{Re}(\hat{u}_x \cdot \hat{u}_z^*) \right] \mathrm{d}A_{\mathrm{R}} , \\ F_y = \vec{F} \cdot \vec{e}_y &= \int_{\mathrm{R}} \frac{1}{4} \frac{y}{a_{\mathrm{R}}} \left[\rho_0 \mathrm{Re}\left(\hat{\vec{u}} \cdot \hat{\vec{u}}^*\right) - \frac{1}{\rho_0 c_s^2} \mathrm{Re}(\hat{p} \cdot \hat{p}^*) \right] \mathrm{d}A_{\mathrm{R}} \\ &\quad - \frac{\rho_0}{2} \int_{\mathrm{R}} \left[\frac{x}{a_{\mathrm{R}}} \mathrm{Re}\left(\hat{u}_y \cdot \hat{u}_x^*\right) + \frac{y}{a_{\mathrm{R}}} \mathrm{Re}\left(\hat{u}_y \cdot \hat{u}_y^*\right) + \frac{z}{a_{\mathrm{R}}} \mathrm{Re}\left(\hat{u}_y \cdot \hat{u}_z^*\right) \right] \mathrm{d}A_{\mathrm{R}} , \\ F_z = \vec{F} \cdot \vec{e}_z &= \int_{\mathrm{R}} \frac{1}{4} \frac{z}{a_{\mathrm{R}}} \left[\rho_0 \mathrm{Re}\left(\hat{\vec{u}} \cdot \hat{\vec{u}}^*\right) - \frac{1}{\rho_0 c_s^2} \mathrm{Re}(\hat{p} \cdot \hat{p}^*) \right] \mathrm{d}A_{\mathrm{R}} \\ &\quad - \frac{\rho_0}{2} \int_{\mathrm{R}} \left[\frac{x}{a_{\mathrm{R}}} \mathrm{Re}(\hat{u}_z \cdot \hat{u}_x^*) + \frac{y}{a_{\mathrm{R}}} \mathrm{Re}\left(\hat{u}_z \cdot \hat{u}_y^*\right) + \frac{z}{a_{\mathrm{R}}} \mathrm{Re}(\hat{u}_z \cdot \hat{u}_z^*) \right] \mathrm{d}A_{\mathrm{R}} , \end{aligned} \tag{D.2}$$

and

$$\begin{aligned} T_x = \vec{T} \cdot \vec{e}_x &= -\frac{\rho_0}{2} \int_{\mathrm{R}} \frac{xy}{a_{\mathrm{R}}} \mathrm{Re}(\hat{u}_x \cdot \hat{u}_z^*) + \frac{y^2 - z^2}{a_{\mathrm{R}}} \mathrm{Re}\left(\hat{u}_y \cdot \hat{u}_z^*\right) \\ &\quad + \frac{yz}{a_{\mathrm{R}}} \mathrm{Re}(\hat{u}_z \cdot \hat{u}_z^*) - \frac{x^2}{a_{\mathrm{R}}} \mathrm{Re}\left(\hat{u}_x \cdot \hat{u}_y^*\right) - \frac{yz}{a_{\mathrm{R}}} \mathrm{Re}\left(\hat{u}_y \cdot \hat{u}_y^*\right) \mathrm{d}A_{\mathrm{R}} , \\ T_y = \vec{T} \cdot \vec{e}_y &= -\frac{\rho_0}{2} \int_{\mathrm{R}} \frac{xz}{a_{\mathrm{R}}} \mathrm{Re}(\hat{u}_x \cdot \hat{u}_x^*) + \frac{yz}{a_{\mathrm{R}}} \mathrm{Re}\left(\hat{u}_x \cdot \hat{u}_y^*\right) \\ &\quad + \frac{z^2 - x^2}{a_{\mathrm{R}}} \mathrm{Re}(\hat{u}_x \cdot \hat{u}_z^*) - \frac{xy}{a_{\mathrm{R}}} \mathrm{Re}\left(\hat{u}_y \cdot \hat{u}_z^*\right) - \frac{xz}{a_{\mathrm{R}}} \mathrm{Re}(\hat{u}_z \cdot \hat{u}_z^*) \mathrm{d}A_{\mathrm{R}} , \\ T_z = \vec{T} \cdot \vec{e}_z &= -\frac{\rho_0}{2} \int_{\mathrm{R}} \frac{x^2 - y^2}{a_{\mathrm{R}}} \mathrm{Re}\left(\hat{u}_x \cdot \hat{u}_y^*\right) + \frac{xy}{a_{\mathrm{R}}} \mathrm{Re}\left(\hat{u}_y \cdot \hat{u}_y^*\right) \\ &\quad + \frac{xz}{a_{\mathrm{R}}} \mathrm{Re}\left(\hat{u}_y \cdot \hat{u}_z^*\right) - \frac{xy}{a_{\mathrm{R}}} \mathrm{Re}(\hat{u}_x \cdot \hat{u}_x^*) - \frac{yz}{a_{\mathrm{R}}} \mathrm{Re}(\hat{u}_x \cdot \hat{u}_z^*) \mathrm{d}A_{\mathrm{R}} . \end{aligned} \tag{D.3}$$

Here $\hat{p}$ and $\hat{\vec{u}} = \left(\hat{u}_x, \hat{u}_y, \hat{u}_z\right)$ are the complex amplitudes of acoustic pressure and particle velocity, respectively. $\vec{e}_x$, $\vec{e}_y$, and $\vec{e}_z$ are unit vectors along the corresponding axes.

References

[1] G. Destgeer, B. H. Ha, J. H. Jung, H. J. Sung, Submicron separation of microspheres via travelling surface acoustic waves, Lab on a Chip 14 (24) (2014) 4665–4672.

[2] M. Wu, Y. Ouyang, Z. Wang, R. Zhang, P.-H. Huang, C. Chen, H. Li, P. Li, D. Quinn, M. Dao, et al., Isolation of exosomes from whole blood by integrating acoustics and microfluidics, Proceedings of the National Academy of Sciences 114 (40) (2017) 10584–10589.

[3] C. M. G. Atehortúa, N. Pérez, M. A. B. Andrade, L. O. V. Pereira, J. C. Adamowski, Water-in-oil emulsions separation using an ultrasonic standing wave coalescence chamber, Ultrasonics sonochemistry 57 (2019) 57–61.

[4] T. Tang, B. Dong, L. Huang, Agglomeration of particles by a converging ultrasound field and their quantitative assessments, Ultrasonics Sonochemistry (2021) 105590.

[5] A. Marzo, S. A. Seah, B. W. Drinkwater, D. R. Sahoo, B. Long, S. Subramanian, Holographic acoustic elements for manipulation of levitated objects, Nature communications 6 (1) (2015) 1–7.

[6] M. Prisbrey, B. Raeymaekers, Ultrasound noncontact particle manipulation of three-dimensional dynamic user-specified patterns of particles in air, Physical Review Applied 10 (3) (2018) 034066.

[7] A. Marzo, B. W. Drinkwater, Holographic acoustic tweezers, Proceedings of the National Academy of Sciences 116 (1) (2019) 84–89.

[8] Y. Yang, T. Ma, S. Li, Q. Zhang, J. Huang, Y. Liu, J. Zhuang, Y. Li, X. Du, L. Niu, et al., Self-navigated 3d acoustic tweezers in complex, media based on time reversal, Research 2021.

[9] C. E. Owens, C. W. Shields, D. F. Cruz, P. Charbonneau, G. P. López, Highly parallel acoustic assembly of microparticles into well-ordered colloidal crystallites, Soft Matter 12 (3) (2016) 717–728.

[10] J. P. Armstrong, S. A. Maynard, I. J. Pence, A. C. Franklin, B. W. Drinkwater, M.

M. Stevens, Spatiotemporal quantification of acoustic cell patterning using Voronoï tessellation, Lab on a Chip 19 (4) (2019) 562–573.

[11] Z. Tian, S. Yang, P.-H. Huang, Z. Wang, P. Zhang, Y. Gu, H. Bachman, C. Chen, M. Wu, Y. Xie, et al., Wave number–spiral acoustic tweezers for dynamic and reconfigurable manipulation of particles and cells, Science Advances 5 (5) (2019) eaau6062.

[12] K. Melde, A. G. Mark, T. Qiu, P. Fischer, Holograms for acoustics, Nature 537 (7621) (2016) 518–522.

[13] Y. Zhu, J. Hu, X. Fan, J. Yang, B. Liang, X. Zhu, J. Cheng, Fine manipulation of sound via lossy metamaterials with independent and arbitrary reflection amplitude and phase, Nature communications 9 (1) (2018) 1–9.

[14] Z. Ma, A. W. Holle, K. Melde, T. Qiu, K. Poeppel, V. M. Kadiri, P. Fischer, Acoustic holographic cell patterning in a biocompatible hydrogel, Advanced Materials 32 (4) (2020) 1904181.

[15] Z. Ma, K. Melde, A. G. Athanassiadis, M. Schau, H. Richter, T. Qiu, P. Fischer, Spatial ultrasound modulation by digitally controlling microbubble arrays, Nature communications 11 (1) (2020) 1–7.

[16] A. Ozcelik, J. Rufo, F. Guo, Y. Gu, P. Li, J. Lata, T. J. Huang, Acoustic tweezers for the life sciences, Nature methods 15 (12) (2018) 1021–1028.

[17] G. Destgeer, A. Hashmi, J. Park, H. Ahmed, M. Afzal, H. J. Sung, Microparticle self-assembly induced by travelling surface acoustic waves, RSC advances 9 (14) (2019) 7916–7921.

[18] D. Foresti, K. T. Kroll, R. Amissah, F. Sillani, K. A. Homan, D. Poulikakos, J. A. Lewis, Acoustophoretic printing, Science advances 4 (8) (2018) eaat1659.

[19] Y. Wang, R. Wu, V. B. Varma, Z. Wang, Y. Seah, Z. Wang, R. Ramanujan, Flowing label-free bacteria trapped by small magnetic fields, Sensors and Actuators B: Chemical 260 (2018) 657–665.

[20] A. Ashkin, J. M. Dziedzic, J. E. Bjorkholm, S. Chu, Observation of a single-beam gradient force optical trap for dielectric particles, Optics letters 11 (5) (1986) 288–

290.

[21] O. M. Maragò, P. H. Jones, P. G. Gucciardi, G. Volpe, A. C. Ferrari, Optical trapping and manipulation of nanostructures, Nature nanotechnology 8 (11) (2013) 807.

[22] D. Choudhary, A. Mossa, M. Jadhav, C. Cecconi, Bio-molecular applications of recent developments in optical tweezers, Biomolecules 9 (1) (2019) 23.

[23] A. Riaud, M. Baudoin, O. B. Matar, L. Becerra, J.-L. Thomas, Selective manipulation of microscopic particles with precursor swirling Rayleigh waves, Physical Review Applied 7 (2) (2017) 024007.

[24] P. J. Westervelt, The theory of steady forces caused by sound waves, The Journal of the Acoustical Society of America 23 (3) (1951) 312–315.

[25] P. J. Westervelt, Acoustic radiation pressure, The Journal of the Acoustical Society of America 29 (1) (1957) 26–29.

[26] G. Maidanik, Torques due to acoustical radiation pressure, The Journal of the Acoustical Society of America 30 (7) (1958) 620–623.

[27] M. Baudoin, J.-L. Thomas, Acoustic tweezers for particle and fluid micromanipulation, Annual Review of Fluid Mechanics 52 (2020) 205–234.

[28] L. Rayleigh, On the momentum and pressure of gaseous vibrations, and on the connection with the virial theorem, Phil. Mag. 3 (1902) 338–346.

[29] K. H. Lam, H.-S. Hsu, Y. Li, C. Lee, A. Lin, Q. Zhou, E. S. Kim, K. K. Shung, Ultrahigh frequency lensless ultrasonic transducers for acoustic tweezers application, Biotechnology and bioengineering 110 (3) (2013) 881–886.

[30] D. Foresti, D. Poulikakos, Acoustophoretic contactless elevation, orbital transport and spinning of matter in air, Physical review letters 112 (2) (2014) 024301.

[31] A. Marzo, M. Caleap, B. W. Drinkwater, Acoustic virtual vortices with tunable orbital angular momentum for trapping of Mie particles, Physical review letters 120 (4) (2018) 044301.

[32] L. P. Gor'kov, Forces acting on a small particle in an acoustic field within an ideal fluid, Doklady Akademii Nauk 140 (1) (1961) 88–91.

[33] B. W. Drinkwater, Dynamic-field devices for the ultrasonic manipulation of microparticles, Lab on a Chip 16 (13) (2016) 2360–2375.

[34] G. T. Silva, Acoustic radiation force and torque on an absorbing compressible particle in an inviscid fluid, The Journal of the Acoustical Society of America 136 (5) (2014) 2405–2413.

[35] E. G. Williams, Fourier acoustics: sound radiation and nearfield acoustical holography, Academic press, 1999.

[36] G. T. Silva, An expression for the radiation force exerted by an acoustic beam with arbitrary wavefront (L), The Journal of the Acoustical Society of America 130 (6) (2011) 3541–3544.

[37] G. Silva, T. Lobo, F. Mitri, Radiation torque produced by an arbitrary acoustic wave, EPL (Europhysics Letters) 97 (5) (2012) 54003.

[38] J. H. Lopes, M. Azarpeyvand, G. T. Silva, Acoustic interaction forces and torques acting on suspended spheres in an ideal fluid, IEEE transactions on ultrasonics, ferroelectrics, and frequency control 63 (1) (2015) 186–197.

[39] T. Tang, L. Huang, Acoustic radiation force for multiple particles over a wide size-scale by multiple ultrasound sources, Journal of Sound and Vibration (2021) 116256, doi:https://doi.org/10.1016/j.jsv.2021.116256.

[40] P. A. Martin, Multiple scattering: interaction of time-harmonic waves with N obstacles, Cambridge University Press, 2006.

[41] P. Hahn, I. Leibacher, T. Baasch, J. Dual, Numerical simulation of acoustofluidic manipulation by radiation forces and acoustic streaming for complex particles, Lab on a Chip 15 (22) (2015) 4302–4313.

[42] D. Ahmed, A. Ozcelik, N. Bojanala, N. Nama, A. Upadhyay, Y. Chen, W. Hanna-Rose, T. J. Huang, Rotational manipulation of single cells and organisms using acoustic waves, Nature communications 7 (1) (2016) 1–11.

[43] F. Mitri, Axisymmetric scattering of an acoustical Bessel beam by a rigid fixed spheroid, IEEE Transactions on Ultrasonics, Ferroelectrics, and Frequency Control 62 (10) (2015) 1809–1818.

[44] F. Mitri, Acoustic scattering of a Bessel vortex beam by a rigid fixed spheroid, Annals of Physics 363 (2015) 262–274.

[45] F. Mitri, Acoustic radiation force on oblate and prolate spheroids in Bessel beams, Wave Motion 57 (2015) 231–238.

[46] F. Mitri, Acoustical pulling force on rigid spheroids in single Bessel vortex tractor beams, EPL (Europhysics Letters) 112(3) (2015) 34002.

[47] F. Mitri, Axial acoustic radiation force on rigid oblate and prolate spheroids in Bessel vortex beams of progressive, standing and quasi-standing waves, Ultrasonics 74 (2017) 62–71.

[48] F. Mitri, Radiation forces and torque on a rigid elliptical cylinder in acoustical plane progressive and (quasi) standing waves with arbitrary incidence, Physics of Fluids 28 (7) (2016) 077104.

[49] F. Mitri, Radiation force and torque on perfect electrically–conducting (PEC) corrugated circular and elliptical cylinders in TE or TM polarized plane progressive waves with arbitrary incidence, Journal of Quantitative Spectroscopy and Radiative Transfer 235 (2019) 15–23.

[50] G. T. Silva, B. W. Drinkwater, Acoustic radiation force exerted on a small spheroidal rigid particle by a beam of arbitrary wavefront: Examples of traveling and standing plane waves, The Journal of the Acoustical Society of America 144 (5) (2018) EL453–EL459.

[51] J. P. Leão-Neto, J. H. Lopes, G. T. Silva, Acoustic radiation torque exerted on a subwavelength spheroidal particle by a traveling and standing plane wave, The Journal of the Acoustical Society of America 147 (4) (2020) 2177–2183.

[52] E. B. Lima, J. P. Leão-Neto, A. S. Marques, G. C. Silva, J. H. Lopes, G. T. Silva, Nonlinear interaction of acoustic waves with a spheroidal particle: Radiation force and torque effects, Physical Review Applied 13 (6) (2020) 064048.

[53] V. A. Erma, An exact solution for the scattering of electromagnetic waves from conductors of arbitrary shape. i. case of cylindrical symmetry, Physical Review 173 (5) (1968) 1243.

[54] G. Gaunaurd, Sonar cross sections of bodies partially insonified by finite sound beams, IEEE journal of oceanic engineering 10 (3) (1985) 213–230.

[55] E. Yamashita, Analysis methods for electromagnetic wave problems, Chapt. 5 Spatial network method.

[56] P. Glynne-Jones, P. P. Mishra, R. J. Boltryk, M. Hill, Efficient finite element modeling of radiation forces on elastic particles of arbitrary size and geometry, The Journal of the Acoustical Society of America 133 (4) (2013) 1885–1893.

[57] Z. Fan, D. Mei, K. Yang, Z. Chen, Acoustic radiation torque on an irregularly shaped scatterer in an arbitrary sound field, The Journal of the Acoustical Society of America 124 (5) (2008) 2727–2732.

[58] D. T. DiPerna, T. K. Stanton, Sound scattering by cylinders of noncircular cross section: A conformal mapping approach, The Journal of the Acoustical Society of America 96 (5) (1994) 3064–3079.

[59] D. B. Reeder, T. K. Stanton, Acoustic scattering by axisymmetric finite-length bodies: An extension of a two-dimensional conformal mapping method, The Journal of the Acoustical Society of America 116 (2) (2004) 729–746.

[60] G. Xu, G. V. Eleftheriades, S. V. Hum, Approach to the analysis and synthesis of cylindrical metasurfaces with noncircular cross sections based on conformal transformations, Physical Review B 102 (24) (2020) 245305.

[61] P. M. Morse, H. Feshbach, Methods of theoretical physics, American Journal of Physics 22 (6) (1954) 410–413.

[62] P. Martin, Two-dimensional acoustic scattering, conformal mapping, and the rayleigh hypothesis, The Journal of the Acoustical Society of America 132 (4) (2012) 2184–2188.

[63] G. B. Arfken, H. J. Weber, Mathematical methods for physicists (1999).

[64] T. Tang, L. Huang. Soundiation: A multi-functional GUI-based software in evaluation of the acoustophoresis by the acoustic radiation force and torque on arbitrary axisymmetric objects. arXiv preprint arXiv:2202.04526 (2022).

[65] M. Settnes, H. Bruus, Forces acting on a small particle in an acoustical feld in a

viscous fluid, Physical Review E 85 (1) (2012) 016327.

[66] C. P. Lee, T. G. Wang, Near-boundary streaming around a small sphere due to two orthogonal standing waves, The Journal of the Acoustical Society of America 85 (3) (1989) 1081–1088.

[67] L. Rayleigh, On the circulation of air observed in Kundt's tubes, and on some allied acoustical problems, Philosophical Transactions of the Royal Society of London 175 (1884) 1–21.

[68] L. D. Landau, E. M. Lifshitz, Course of theoretical physics, Elsevier, 2013.